

1 **Auditory brainstem models: adapting cochlear nuclei improve**
2 **spatial encoding by the medial superior olive in reverberation**

3 **Andrew Brughera^{1,2‡*}, Jason Mikiel-Hunter^{1‡}, Mathias Dietz³, David McAlpine¹**

4 ¹ Department of Linguistics, and the Australian Hearing Hub, Macquarie University,
5 Macquarie Park, New South Wales, Australia

6 ² Department of Biomedical Engineering, Boston University,
7 Boston, Massachusetts, United States of America

8 ³ Medizinische Physik and Cluster of Excellence "Hearing4all", Universität Oldenburg,
9 Oldenburg, Lower Saxony, Germany

10 ‡ A.B. and J.M.H. contributed equally to this work.

11

12 * Corresponding author:

13 Andrew Brughera

14 andrew.brughera@mq.edu.au

15

16 ORCID information:

17 Andrew Brughera: <https://orcid.org/0000-0002-2461-3894>

18 Jason Mikiel-Hunter: <https://orcid.org/0000-0002-6085-9269>

19 Mathias Dietz: <https://orcid.org/0000-0002-1830-469X>

20 David McAlpine: <https://orcid.org/0000-0001-5467-6725>

21

22 Abstract: 209 words

23 Introduction: 681 words

24 Discussion: 1735 words

25 Number of tables: 2

26 Number of figures: 8, plus 1 supplemental figure

27

28 Abstract

29 Listeners perceive sound-energy as originating from the direction of its source, even as direct
30 sound is followed milliseconds later by reflected sound from multiple different directions. Early-
31 arriving sound is emphasised in the ascending auditory pathway, including the medial superior
32 olive (MSO) where binaural neurons encode the interaural time difference (ITD) cue for spatial
33 location. Behaviourally, weighting of ITD conveyed during rising sound-energy is stronger at
34 600 Hz, a frequency with higher reverberant energy, than at 200 Hz where reverberant energy
35 is lower. Here we computationally explore the combined effectiveness of adaptation before
36 ITD-encoding, and excitatory binaural coincidence detection within MSO neurons, in
37 emphasising ITD conveyed in early-arriving sound. With excitatory inputs from adapting model
38 spherical bushy cells (SBCs) of the bilateral cochlear nuclei, a Hodgkin-Huxley-type model
39 MSO neuron reproduces the frequency-dependent emphasis of rising vs. peak sound-energy
40 in ITD-encoding. Maintaining the adaptation in model SBCs, and adjusting membrane speed in
41 model MSO neurons, hemispheric populations of model SBCs and MSO neurons, with
42 simplified membranes for computational efficiency, also reproduce the stronger weighting of
43 ITD information conveyed during rising sound-energy at 600 Hz compared to 200 Hz. This
44 hemispheric model further demonstrates a link between strong weighting of spatial information
45 during rising sound-energy, and correct unambiguous lateralisation of reverberant speech.

46 **Keywords**

47 adaptation; cochlear nucleus; MSO; binaural; sensory coding; spatial hearing

48 **Declarations**

49 ***Funding***

50 This work was supported by Australian Research Council Laureate Fellowship (FL160100108) awarded
51 to David McAlpine

52 ***Conflicts of interest/Competing interests***

53 The authors declare that they have no conflict of interest, and no competing interest.

54 ***Ethics approval***

55 For this strictly computational study, no approval was required.

56 ***Consent to participate***

57 For this strictly computational study, no consent was required.

58 ***Consent for publication***

59 For this strictly computational study, there are no human subjects from whom consent is required. All
60 authors and responsible authorities approve the publication of this manuscript.

61 ***Availability of data and material***

62 For the nonlinear model: data, analysis scripts, and code are available at figshare:

63 <https://doi.org/10.6084/m9.figshare.11955219.v1>

64 For the linear model: data, analysis scripts, and code are available at figshare:

65 <https://doi.org/10.6084/m9.figshare.9899018.v1>

66 ***Code availability***

67 For the nonlinear model: code is available at Github:

68 https://github.com/AndrewBrughera/Mso_SbcStp_EE1

69 For the linear model: code is available at figshare: <https://doi.org/10.6084/m9.figshare.9899018.v1>

70 ***Author Contributions***

71 Andrew Brughera & Jason Mikiel-Hunter contributed equally.

72 **Conceptualisation:** David McAlpine & Mathias Dietz

73 **Data Curation:** Jason Mikiel-Hunter & Andrew Brughera

74 **Formal Analysis:** Jason Mikiel-Hunter & Andrew Brughera

75 **Funding Acquisition:** David McAlpine

76 **Investigation:** Andrew Brughera & Jason Mikiel-Hunter

77 **Methodology:** Andrew Brughera (nonlinear modelling) & Jason Mikiel-Hunter (linear modelling)

78 **Resources:** David McAlpine, Andrew Brughera, & Jason Mikiel-Hunter

79 **Software:** Andrew Brughera & Jason Mikiel-Hunter

80 **Supervision:** David McAlpine

81 **Visualisation:** Jason Mikiel-Hunter & Andrew Brughera

82 **Validation:** Andrew Brughera & Jason Mikiel-Hunter

83 **Writing – Original Draft Preparation:** Andrew Brughera, Jason Mikiel-Hunter, & David McAlpine

84 **Writing – Review & Editing:** Andrew Brughera, David McAlpine, Mathias Dietz, & Jason Mikiel-Hunter

85 Introduction

86 Sound propagating directly from its source to a listener's ears is typically followed milliseconds
87 later by multiple reverberant copies arriving from different directions (Fig. 1). Despite this
88 mixture of direct and reflected sound pressure, generating non-stationary spatial information in
89 the binaural cues—interaural time differences (ITDs) and interaural intensity differences
90 (IIDs)—listeners typically perceive a sound as punctate, and originating from the direction of its
91 source (Dietz et al., 2013). Perception of the true location of the source can persist even when
92 the intensity of reflected sound matches or exceeds that of early-arriving, direct sound (Haas,
93 1951), facilitating 'cocktail party listening': attending to a single talker against a background of
94 many competing voices (Cherry, 1953).

95 Behavioural emphasis of early-arriving ITD information is frequency dependent (Hu et al.,
96 2017): for amplitude-modulated 600-Hz sounds, listeners are more sensitive to ITDs conveyed
97 during the rising-energy portion than they are to ITDs at the energy peak; this is not the case at
98 200 Hz, where listeners are equally sensitive to ITDs conveyed during rising and peak energy.
99 Acoustically, reverberant energy can be 20 dB less intense at 200 Hz than at 600 Hz in many
100 outdoor settings (Traer & McDermott, 2016). For both frequencies, listeners are least sensitive
101 to ITD during falling sound-energy, when direct sound is most likely to be corrupted by
102 reverberation. These data suggest that spatial auditory brain mechanisms transmit reliable
103 information, and suppress unreliable information, accounting for natural frequency-profiles in
104 reverberant energy which decrease below 1500 Hz.

105 Neural emphasis of early-arriving sound is observed in the auditory nerve, brainstem,
106 midbrain, and auditory cortex (Dietz et al., 2014; Fitzpatrick et al., 1999; Liebenthal & Pratt,
107 2002; Litovsky & Yin, 1998a, 1998b). In the brainstem, medial superior olive (MSO) neurons,
108 performing binaural coincidence detection that encodes ITDs in low-frequency sounds
109 (Mathews et al., 2010; Yin & Chan, 1990), respond strongest to their preferred ITD during
110 rising sound-energy in amplitude-modulated binaural beats (AMBBs), producing an emphasis
111 of early-arriving spatial information that is consistent with adaptation in monaural projection
112 pathways to binaural MSO neurons (Dietz et al., 2014). Within these pathways, MSO neurons
113 receive bilateral excitation from spherical bushy cells (SBCs) of the ventral cochlear nuclei
114 (VCN) (Smith et al., 1993). Each SBC is driven by 1-3 auditory nerve fibres (ANFs), each
115 terminating in a calyceal Endbulb of Held synapse (Lorente De No, 1981). Potential adaptive
116 mechanisms include: spike-rate adaptation in ANFs (Moser & Beutner, 2000; Zilany & Carney,
117 2010); short-term plasticity (STP, synaptic depression) observed *in vitro* at the synapse from
118 ANF to SBC (Oleskevich et al., 2000; Wang & Manis, 2008; Yang & Xu-Friedman, 2009,
119 2015); and glycinergic inhibition at SBCs observed *in vivo* (Keine & Rübtsamen, 2015; Keine et
120 al., 2016; Kuenzel et al., 2011, 2015).

121 Here we present simplified computational models of the auditory brainstem (Figs. 2 and 5),
122 exploring the combined effectiveness of monaural adaptation, and excitatory binaural

123 coincidence detection, in emphasising ITD conveyed in early-arriving sound, and improving the
124 lateralisation of speech in reverberation. In our simplified models, adapting ANFs (Zilany et al.,
125 2014, 2009) drive SBCs (Rothman & Manis, 2003c) that adapt according to the STP *in vitro*;
126 despite weak STP *in vivo* (Keine et al., 2016; Kuenzel et al., 2011), nearly identical temporal
127 properties to the inhibition *in vivo* (Kuenzel et al., 2015; Wang & Manis, 2008) support
128 expected adaptive effects. With excitatory inputs from the adapting model SBCs, a Hodgkin-
129 Huxley-type model MSO neuron reproduces *in vivo* AMBB-responses of MSO neurons and the
130 frequency-dependent emphasis of rising vs. peak sound-energy in ITD-encoding (Dietz et al.,
131 2014; Hu et al., 2017). Maintaining the adaptation in model SBCs, and adjusting membrane
132 speed in model MSO neurons within the observed range (Bondy & Golding, 2018; Remme et
133 al., 2014; Scott et al., 2007), hemispheric populations of model SBCs and MSO neurons, with
134 simplified membranes for computational efficiency, also reproduce the stronger weighting of
135 ITD conveyed during rising sound-energy at 600 Hz compared to 200 Hz. This hemispheric
136 model further demonstrates a link between strong weighting of spatial information during rising
137 sound-energy, and correct unambiguous lateralisation of reverberant speech (Haas, 1951).

138

139 **Methods**

140 ***Nonlinear brainstem model***

141 This computational model (Fig. 2B) incorporates an MSO neuron and its excitatory input
142 pathways, beginning with an auditory periphery model for humans (Glasberg & Moore, 1990;
143 Zilany et al., 2014), with 12 left and 12 right adapting model ANFs of medium spontaneous
144 rate. Three model ANFs drive each adapting model SBC of the VCN (Rothman & Manis,
145 2003c; Rudnicki & Hemmert, 2017). Four left and four right SBCs project excitatory synaptic
146 inputs to a multi-compartment model MSO neuron (Brughera et al., 2013). Acoustic stimuli and
147 the auditory periphery model are implemented in Matlab (Natick, Massachusetts, USA)
148 (www.mathworks.com). Model SBCs and MSO neuron are Hodgkin-Huxley-type (Hodgkin &
149 Huxley, 1952), implemented in the Python 3.7 Brian2 Neural Simulator (Stimberg et al., 2019).
150 Code is available at Github: https://github.com/AndrewBrughera/Mso_SbcStp_EE1
151 Data, analysis scripts, and code are available at figshare:
152 <https://doi.org/10.6084/m9.figshare.11955219.v1>

153 ***Acoustic Stimuli***

154 Acoustic stimuli are amplitude-modulated binaural beats (AMBBs) (Fig. 2A) (Dietz et al., 2013)
155 at 75 dB SPL RMS at peak amplitude, in which binaurally presented tones of a slightly different
156 frequency are modulated in amplitude at a rate equal to the difference in frequency across the
157 two ears. With this stimulus, each cycle of rising and falling sound-energy contains a full cycle
158 of interaural phase disparities.

159 ***Auditory Periphery Model***

160 The acoustic stimuli are processed by an auditory periphery model for humans (Glasberg &
161 Moore, 1990; Zilany et al., 2014). Peripheral processing includes 24 adapting ANFs of medium
162 spontaneous rate: 12 each in the left and right ears, with a 200-Hz or 600-Hz characteristic
163 frequency (CF, the frequency at which a neuron fires above spontaneous rate for the lowest
164 sound pressure level, SPL). CF results from the frequency-tuning of the inner ear, and the CFs
165 of ANFs distally driving a neuron.

166 ***Model SBCs***

167 SBCs (Type II VCN neurons) are modelled as Hodgkin-Huxley-type point neurons (Rothman &
168 Manis, 2003c), adjusted for temperature 37°C) with three independent, excitatory synapses
169 each driven by a model ANF (Lorente De No, 1981). Each model synapse is an excitatory
170 synaptic conductance ($g_{E_{SBC}}$) in series with an excitatory reversal potential of 0 mV. Each input
171 spike causes a variable increment in its synapse's excitatory conductance (with a standard
172 unadapted maximum increment, or maximum excitatory synaptic strength, $\Delta g_{E_{SBC}} = 83$ nS;
173 spike-threshold was 34 nS for a single input from rest, using the same model membrane and
174 faster synapses at 38°C (Rothman & Manis, 2003c)). $g_{E_{SBC}}$ then decays exponentially with
175 time-constant 0.2 ms (Kuenzel et al., 2011, 2015). The increment (i.e., the synaptic strength) is

176 variable due to depression at the individual synapses, modelled as in Rudnicki & Hemmert
177 (2017): immediately after an input spike and its associated increment in excitatory
178 conductance, the synaptic strength is multiplied by $1 - u$, where $u = 0.5$. This synaptic
179 depression recovers exponentially with time-constant 25 ms, as measured *in vitro* (Wang &
180 Manis, 2008). Low synchrony to amplitude modulation (AM) in the model SBCs is consistent
181 with the auditory nerve at high SPL (Joris & Yin, 1992) and lower synchrony in primary-like
182 neurons of the cochlear nuclei (Rhode & Greenberg, 1994). Compared with a single input,
183 three inputs per model SBC increased spike rates, reduced synchrony to AM, and supported a
184 small number of excitatory inputs (Couchman et al., 2010) to the model MSO neuron.

185 *Model MSO neuron*

186 The Hodgkin-Huxley-type model principal MSO neuron has separate compartments
187 representing the bilateral dendrites, soma, and axon (Zhou et al., 2005). The model axon
188 functions simply as a spike generator, without myelination or Nodes of Ranvier. Compared with
189 a previous model (Brughera et al., 2013), the soma is simplified being spherical and iso-
190 potential, and the somatic and dendritic membrane conductances for voltage-sensitive ion-
191 channels are scaled by 0.6. Models for fast-acting ion-channels, the low-threshold potassium
192 (K_{LT}) channels (Mathews et al., 2010) and sodium (Na) channels (Scott et al., 2010) are based
193 on the MSO. The model for slowly-varying hyperpolarization-activated cyclic nucleotide (H)
194 channels remains based on the VCN (Rothman & Manis, 2003c).

195 On the bilateral model dendrites, eight excitatory synapses (Couchman et al., 2010) are
196 located one each at 42.5, 47.5, 52.5, and 57.5% of the dendritic length. Each synapse is
197 modelled as a variable conductance ($g_{E_{MSO}}$) in series with an excitatory reversal potential (V_E)
198 of 0 mV. Noting that STP in the brainstem is weak *in vivo* (Keine et al., 2016; Kuenzel et al.,
199 2011; Lorteije et al., 2009; Yin & Chan, 1990), the synapses are non-depressing. Each
200 synapse is driven by a single model SBC from the same side. An input spike increments its
201 synaptic conductance by a fixed amount (the excitatory synaptic strength, $\Delta g_{E_{MSO}}$), and the
202 conductance then decays exponentially with time-constant $\tau_E = 0.4$ ms, within physiological
203 range (Fischl et al., 2012; Franken et al., 2015). With inputs from adapting SBCs (results in
204 Figs. 3B and 4), $\Delta g_{E_{MSO}} = 36$ nS, comparable with excitatory fibre conductances of 37 ± 4 nS
205 measured *in vitro* (Couchman et al., 2010).

206 Membrane parameters for each compartment (Table 1) are given below. Certain parameters
207 (Table 2) were adjusted for the conditions yielding results shown in Figs. 3-4. $V_{AP-THRESHOLD}$ is a
208 fixed threshold for counting action potentials: when the membrane voltage near the midpoint of
209 the model axon transitions from -35 mV or less to greater than -20 mV, a spike is counted; this
210 threshold is simply for counting, and does not affect the operation of the model. The somatic
211 membrane time-constant of 0.39 ms was calculated from measured membrane impedance in
212 the model (see below and Supplemental Fig. S1).

213 **Table 1. Model MSO neuron: compartmental and membrane parameters**

Parameter	Dendrites (2)	Soma	Axon
Temperature (°C)	37	37	37
Number of sub-compartments	20	2	51
Diameter (μm)	3.5	30	2
Length (μm)	150	30	400
Resistivity, R_S (ohm x cm)	150	0	150
C_M (μF/cm ²)	1	1	1
V_{KLT} (mV)	-106	-106	-106
V_{Na} (mV)	n/a	+62.1	+62.1
V_H (mV)	-43	-43	-43
V_L (mV)	-65	-65	-65
g_{maxKLT} (S/cm ²)	0.00132	0.0324	0.0595
g_{maxNa} (S/cm ²)	0 (none)	0.0432	0.25
g_{maxH} (S/cm ²)	0.00066	0.01296	0.0025
g_L (S/cm ²)	0.00005	0.00005	0.00005
V_E (mV)	0	n/a	n/a
$V_{AP-THRESHOLD}$ (mV, set)	n/a	n/a	-20
V_{REST} (mV, measured)	-60.53	-60.52	-64.35

214

215 **Table 2. Excitatory synaptic parameters**

Results shown in:	Fig. 3A	Figs. 3B & 4
Model SBCs	control	test
Full Synaptic Strength, Δg_{ESBC} (nS)	400	83
Synaptic Time-Constant, τ_{ESBC} (ms)	0.2	0.2
Synaptic Depression, u	0 (none)	0.5
Recovery Time-Constant (ms)	n/a	25
Model MSO neurons	control	test
Synaptic Strength, Δg_{EMSO} (nS)	21	36
Synaptic Time-Constant, τ_{EMSO} (ms)	0.4	0.4

216

217 Within this model MSO neuron, its functional electric-circuit unit, the sub-compartment (Fig.
218 2C), connects to its neighbouring sub-compartments via series resistivity (R_s) representing the
219 neuron's internal cytoplasm. Within each sub-compartment, the neural membrane is modelled
220 as a transmembrane capacitance (C_M) in parallel with ion-channel populations: Na, H, K_{LT} , and
221 leakage (L). Each ion-channel population is represented as a reversal potential (V_{Na} , V_H , V_{KLT} ,
222 V_L) in series with a conductance (g_{Na} , g_H , g_{KLT} , g_L). With the exception of a fixed leakage
223 conductance (g_L) representing voltage-insensitive ion channels, each conductance value is
224 equal to a maximum conductance multiplied by voltage-sensitive activation and inactivation
225 gating variables with integer exponents (Hodgkin & Huxley, 1952).

226 Kirchhoff's current equation, applied to the model MSO neuron, states that the sum of currents
227 entering any point is zero:

$$228 \quad 0 = i_{C_M} + i_{Na} + i_{K_{LT}} + i_H + i_L + i_{S1} + i_{S2}$$

229 Series currents, i_{S1} and i_{S2} , are calculated by the Brian2 simulator according to the voltage
230 differences, resistivity, and geometry of the related sub-compartments.

231 Capacitive membrane current (i_{C_M}) increases with membrane capacitance and the time-
232 derivative of membrane potential V :

$$233 \quad i_{C_M} = C_M \frac{dV}{dt}.$$

234 Leakage current: $i_L = g_L(V - V_L)$.

235 Na current (Scott et al., 2010), which is rapidly varying, is based on the MSO:

$$236 \quad i_{Na} = g_{Na}(V - V_{Na}).$$

$$237 \quad g_{Na} = gmax_{Na}m^4(0.993h + 0.007).$$

238 Each voltage-sensitive ionic conductance has a constant maximum conductance value ($gmax$)
239 (Table 1), and has voltage and time dependencies defined by a subset of the activation and
240 inactivation variables m , h , w , z , and r , each with a rate of change governed by a first-order
241 differential equation with a time-constant divided by the Q_{10} temperature factor of $3^{(T-22)/10}$,
242 where T is set equal to human body temperature, 37°C. For Na channels:

$$243 \quad \frac{dm}{dt} = Q_{10}(m_{\infty} - m)/\tau_m$$

$$244 \quad \frac{dh}{dt} = Q_{10}(h_{\infty} - h)/\tau_h$$

245 For model Na channels, steady-state activation (m_{∞}) and inactivation (h_{∞}), and their
246 respective time constants (τ_m and τ_h) in milliseconds, are functions of membrane potential in
247 millivolts (Scott et al., 2010):

248 $m_{\infty} = 1./ (1 + \exp((V + 46.) / (-11.)))$

249 $\tau_m = ((0.141 + (-0.0826 / (1 + \exp((-20.5 - V) / 10.8)))) / 3.)$

250 $h_{\infty} = 1./ (1 + \exp((V + 62.5) / 7.77))$

251 $\tau_h = ((4. + (-3.74 / (1 + \exp((-40.6 - V) / 5.05)))) / 3.)$

252 K_{LT} current (Mathews et al., 2010), which is rapidly-varying, is based on the MSO:

253 $i_{KLT} = g_{KLT}(V - V_{KLT}).$

254 $g_{KLT} = gmax_{KLT}w^4z.$

255 $\frac{dw}{dt} = Q_{10}(w_{\infty} - w)/\tau_w$

256 $\frac{dz}{dt} = Q_{10}(z_{\infty} - z)/\tau_z$

257 $w_{\infty} = 1./ (1 + \exp((V + 57.34)/(-11.7)))$

258 $\tau_w = ((21.5/((6.* \exp((V + 60.)/7.)) + (24.* \exp(-1 * (V + 60.)/50.6)))) + 0.35)$

259 $k = 0.27$

260 $z_{\infty} = ((1. - k)/(1 + \exp((V + 67.)/6.16))) + k$

261 $\tau_z = ((170./(5.* \exp((V + 60.)/10.) + \exp((V + 70.)/8.))) + 10.7)$

262 The non-inactivating H current (Rothman & Manis, 2003c), which is slowly-varying, remains
263 based on the VCN:

264 $i_H = g_H(V - V_H).$

265 $g_H = gmax_Hr .$

266 $\frac{dr}{dt} = Q_{10}(r_{\infty} - r)/\tau_r$

267 $r_{\infty} = 1./ (1 + \exp((V + 76.) / 7.))$

268 $\tau_r = ((100000./ (237.* \exp((V + 60.) / 12.) + 17.* \exp(-(V + 60.) / 14.))) + 25.)$

269 Maximum conductance ($gmax$) values are set for plausible resting potentials and membrane
270 time constants. Leakage conductance equals the value of Scott et al. based on measurements
271 from the MSO (Scott et al., 2010). The reversal potential for leakage in the model dendrites
272 and soma is reduced from -60 mV to -65 mV, now consistent with the model axon (Brughera et
273 al., 2013). For voltage-sensitive ion-channels, ratios of the maximum conductances for ion
274 channels are calculated for resting potentials: near -60 mV in the soma and dendrites,

275 consistent with physiological values promoting activation of model K_{LT} channels (Mathews et
276 al., 2010); and near -64 mV in the axon to reduce inactivation of model Na channels. The 4-mV
277 difference produces a small current from soma to axon, calculated at 20 picoamperes (pA),
278 much less than synaptic currents. Although less negative than the -68 mV in a dedicated MSO
279 axon model (Lehnert et al., 2014), the resting potential in our model axon has been shown to
280 support large axonal action potentials, without significant back-propagation to the soma at its
281 higher resting potential and lower ratio of Na to K_{LT} conductance (Brughera et al., 2013), which
282 is consistent with the small somatic action potentials of MSO neurons (Scott et al., 2007). From
283 the calculated ratios of maximum conductance, values are scaled. Model somatic membrane
284 impedance as a function of frequency was measured by simultaneous injection of a
285 transmembrane bias current, and a sinusoidal current containing a linear frequency sweep
286 from 1 to 2000 Hz during a duration of 1 second (Hutcheon & Yarom, 2000; Puil et al., 1986;
287 Remme et al., 2014). Prior to stimulus, the model membrane settled for 0.1 s to its resting
288 potential, -60.52 mV. Settling was followed by a steady inward bias current applied for 0.9 s.
289 The bias current was then maintained as the frequency sweep in membrane current (250-pA
290 peak amplitude) was also applied. A resonance in membrane impedance emerges with
291 increases in bias current (Supplemental Fig. S1). Assuming that the resonant membrane is a
292 second-order system (Nilsson & Riedel, 2008), the membrane time-constant is equal to the
293 reciprocal of angular resonance frequency. With a bias current of 300 pA, resulting in a holding
294 potential of -59.22 mV, the resonance at 408 Hz indicates a membrane time-constant of $1/(2\pi$
295 $\times 408 \text{ Hz}) = 0.390 \text{ ms}$, which is within the range of 0.3 to 0.6 ms measured in principal MSO
296 neurons (Couchman et al., 2010; Scott et al., 2007).

297 *AMBB period histograms*

298 For each AMBB period histogram from the nonlinear model, spikes were counted in forty non-
299 overlapping bins, each covering 1/40 of the AM cycle (unsmoothed). Spike rates were
300 calculated by dividing the spike count by the total time duration for each bin, across the
301 multiple periods of eight different stimulus presentations of 0.75-second duration.

302 *Eight starting-phases at decrements of 45° efficiently implemented IPDs*

303 At each carrier and modulation-frequency combination, 8 acoustic stimuli, each with 1 of 8
304 carrier *starting-phases* (0° , -45° , -90° , ..., -315°), were applied at each model ear, driving
305 ANFs. For computational efficiency, *start-IPD* (the interaural phase difference at zero
306 amplitude) was achieved by pairing spike times from each *starting-phase* in one ear, with the
307 spike times from the other ear having the appropriate difference in *starting-phase*. While
308 maintaining the proper *start-IPD*, each AMBB period histogram pooled spikes resulting from
309 stimuli using the 8 *starting-phases* spanning each carrier period. Thus whilst the histograms
310 show the effects of *start-IPD*, they do not show phase-locking to fine structure of the carriers.

311 In this study, “best-ITD during rise” denotes *start-IPD* = 270° ; “best-ITD at peak” denotes *start-*
312 *IPD* = 180° ; and “best-ITD during fall” denotes *start-IPD* = 90° .

313 *Chi-squared tests for significant differences in model spike counts*

314 For each condition and modulation frequency, a chi-squared test for one and two degrees of
315 freedom (2-way and 3-way comparisons) compared spike counts from the nonlinear model
316 MSO neuron stimulated with AMBBs with best-ITD occurring during rising vs. peak vs. falling
317 amplitude. Each chi-squared test yielded a probability (P) of the null hypothesis that the
318 differences in spike count occurred randomly.

319 *Synchrony index and Rayleigh statistic for significant phase-locking:*

320 For each modulation frequency and *starting-phase* combination, the synchrony index (SI , R) of
321 spike times (t_i) (Johnson, 1980) with respect to their phase θ_i within the AM cycle (with
322 modulation frequency f_m , and modulation period $T_m = 1/f_m$) was calculated:

$$323 \theta_i \triangleq 2\pi f_m \text{mod}(t_i, T_m)$$

$$324 SI = \sqrt{(\sum_{i=1}^N \cos \theta_i)^2 + (\sum_{i=1}^N \sin \theta_i)^2}, \text{ where } N \text{ is the spike count.}$$

325 The Rayleigh significance statistic ($2NR^2$) was then calculated and converted to a P value, the
326 probability of the null hypothesis that the AM period-histogram of spike times resulted from a
327 uniform distribution (Rhode, 1976):

328	P	0.10	0.05	0.025	0.01	0.001
329	$2NR^2$	4.605	5.991	7.378	9.210	13.816

330 *Lateralisation model with Linear-membrane models*

331 To study how monaural adaptation and biophysical profiles could impact lateralisation of
332 acoustic stimuli in anechoic and reverberant conditions, we constructed a model of
333 lateralisation whose brainstem stages (SBCs and MSO neurons) are represented by point
334 neurons with linear biophysical properties (Remme et al., 2014). Data, analysis scripts, and
335 code are available at figshare: <https://doi.org/10.6084/m9.figshare.9899018.v1>

336 Two stimuli were presented to the model: the first, a SAM tone with non-zero ITDs inserted at
337 different phases of the AM cycle, as used behaviourally to determine how carrier frequency
338 affects ITD sensitivity over the time course of an AM cycle (Hu et al., 2017); the second, a
339 natural speech stimulus with early reflections, has been proposed as a simple simulation of a
340 reverberant environment where correct lateralisation is only possible if ITD cues in the onset
341 waveform are processed preferentially (Dietz et al., 2014).

342 *SAM tones with non-zero ITDs inserted at different phases of AM cycle*

343 This stimulus was generated according to the Hu et al. (2017) study that first used it. In
344 summary, SAM tones were created from pulse trains that had been bandpass-filtered and then
345 amplitude-modulated. Non-stationary ITDs were added by temporally shifting individual pulses
346 in one of either the rising, peak or falling phases of the AM cycle. For the purposes of this

347 study, non-stationary ITDs of +300 μ s and +150 μ s were inserted into SAM tones of either
348 200-Hz or 600-Hz carrier frequency respectively. These ITD values were chosen based on
349 individual behavioural thresholds in the Hu et al. (2017) study. At each carrier frequency, four
350 conditions were tested: two different AM frequencies (8 Hz or 20 Hz) and two different
351 proportions of rising, peak or falling AM phases with a non-zero ITD inserted (20% or 40%).
352 These parameters match those tested behaviourally by Hu et al. (2017).

353 *A natural speech stimulus with early reflections*

354 A single monosyllabic consonant-vowel nucleus-consonant (CNC) word token, 'church',
355 (spoken by an Australian-English, female voice), was selected as a stimulus (Fig. 1 and Fig.
356 8). To simulate its arrival from a location one metre away to the right of the midline in an
357 anechoic environment, the word's waveform (normalised at 70dB) was convolved with a large
358 pinnae HRTF for +30° azimuthal location (CIPIC database, UC Davis). A reverberant space
359 was simulated by adding to the direct (+30°) pathway two early reflections off virtual walls
360 stood behind and to the right of the subject (Fig. 1). These reflected copies of the words
361 arrived from -65° and -130° angles (again convolved with large-pinnae HRTFs from the CIPIC
362 database) and were delayed by 4ms and 8ms respectively to reproduce their elongated paths
363 (Dietz et al., 2014).

364 *Linear model circuitry*

365 The linear model, consists of three stages: an initial auditory periphery stage (the middle/inner
366 ear and ANFs) and two brainstem stages (cochlear nuclei and MSO). Unlike the nonlinear
367 model, the linear model incorporates two parallel circuits, representing the 'left' and 'right' MSO
368 nuclei and their inputs. The difference in output rate between these parallel circuits is utilised to
369 calculate lateralisation of the natural stimulus. The only discernible difference between 'left'
370 and 'right' circuits is the contralateral $\frac{1}{8}$ pi shifts in their MSO neurons' IPD tuning curve peaks
371 which are generated by delaying the outputs from the auditory periphery stage ipsilateral to the
372 MSO nucleus in question. This shift is considered physiological given experimentally observed
373 binaural tuning curves from the auditory brainstem whose optimal characteristics have been
374 corroborated theoretically (McAlpine et al., 2001).

375 *Auditory periphery stage*

376 Peripheral processing of the acoustic stimuli in the linear model is performed by a cat
377 middle/inner ear model (Zilany et al., 2014) in Matlab. Outputs from the auditory periphery are
378 restricted to 200-Hz/600-Hz for the pulse-shifted SAM tones (matching their SAM tone's carrier
379 frequency) and 600-Hz for lateralisation of the speech stimulus with early reflections. This
380 latter value was chosen based on it being within the 500-750 Hz frequency range in which
381 temporal-fine-structure (TFS) ITD sensitivity is considered strongest (Ihlefeld & Shinn-
382 Cunningham, 2011). When exploring effects, of synaptic depression at the inputs from
383 auditory nerve to VCN, on the lateralisation of a speech stimulus, the same auditory nerve
384 simulations are used for both the depressing and non-depressing inputs.

385 *Linear-membrane model properties*

386 Single-compartment, linear-membrane models are used to represent both SBC and MSO
387 neurons in the linear model. These linear-membrane models can incorporate two dynamic
388 currents (Remme et al., 2014): I_w , a resonant current and/or, I_n , an amplifying current. The
389 current balance equation for the general neural model is as follows:

$$390 \quad c \frac{dv}{dt} = -g_M v - g_w w_w + g_n w_n + I_{app}(t)$$

391 Where c is capacitance (picofarads), g_M is total membrane conductance (nanosiemens, nS)
392 and I_{app} is the current (picoamperes) applied to the neural model. The resonant and amplifying
393 currents, I_w and I_n , are described by their conductances, g_w and g_n (in nS); the dynamics of
394 their gating variables, w_w and w_n (in millivolts) are described generically by the equation:

$$395 \quad \tau_w \frac{dw_w}{dt} = v - w_w$$

$$396 \quad \tau_w \frac{dw_w}{dt} = v - w_w$$

397 Where w_x is the gating variable whose associated time-constant is τ_x (milliseconds).

398 Two parameter sets are chosen to represent the range of membrane speeds recently
399 observed in MSO neurons (Bondy & Golding, 2018; Remme et al., 2014). These example
400 model membranes can be broadly characterised as either fast with a high resonance-
401 frequency or slow with a low resonance-frequency as previously modelled by Remme et al.
402 (2014). While both fast and slow model membranes are used to represent MSO neurons, only
403 the fast model membrane was chosen to represent all SBCs,

404 *Synaptic properties and plasticity*

405 Providing excitatory drive to each linear model SBC, again 3 independently-simulated ANFs
406 were applied. Excitatory unitary conductances at this synapse are modelled as alpha functions
407 with an exponential time course of 0.2ms. Synaptic depression with a single exponential
408 recovery is also implemented at this stage, with similar parameters values ($u = 0.55$; $\tau = 25$
409 ms) to the Hodgkin-Huxley-type SBCs.

410 Each MSO neuron receives 4 (independently-simulated) excitatory cochlear-nucleus inputs
411 from “either ear” in the linear model. Alpha functions are again used to model the unitary
412 excitatory conductances at this synapse, with time-constants: 0.2 ms paired with slow model
413 membranes, and 0.5 ms paired with slow model membranes. Where comparisons of fast and
414 slow model neurons are made, the same adapting auditory nerve inputs are presented to their
415 respective cochlear-nucleus stages.

416 *Spike thresholds in the linear-membrane model*

417 The linear-membrane model applies idealised spike thresholds (Remme et al., 2014). A slope
418 threshold (dv/dt) is used for all neuronal types. Threshold values for cochlear-nucleus cells are
419 selected to produce good average firing rate without undermining the effects of synaptic
420 depression. Threshold values for the MSO neurons are selected to obtain maximum dynamic
421 range of ITD tuning functions for 200/600 Hz pure tone stimuli (where dynamic range is
422 considered the difference between the maximum and minimum ITD-modulated spike rate). A
423 refractory period of 1 ms is implemented as in Remme et al. (2014) for model SBCs and fast
424 model MSO neurons, whereas a longer refractory period of 2 ms is used for slow model MSO
425 neurons, reflecting longer refractory periods in neurons with lower densities of K_{LT} channels
426 (Rothman & Manis, 2003b, 2003a, 2003c).

427 *Calculating lateralisation using d' values*

428 Lateralisation of a reverberant natural stimulus is judged in the linear model by calculating the
429 mean spike rate difference between a population of 50 'left' and 50 'right' MSO neurons to a
430 single stimulus presentation. d' values are calculated to quantify the degree of separation of
431 'left' and 'right' spike rates using the following equation:

$$432 \quad d' = \frac{\mu_L - \mu_R}{\sqrt{\frac{1}{2}(\sigma_L^2 + \sigma_R^2)}}$$

433 Where μ_L is the mean spike rate for the 'left' population of MSO neurons in 5-ms bins; μ_R is the
434 mean spike rate for the 'right' population of MSO neurons in 5-ms bins; σ_L is the standard
435 deviation of the 'left' MSO population's spike rate and σ_R is the standard deviation of the 'right'
436 population's spike rate (both calculated in 5-ms bins again).

437 The sign and magnitude of the d' allows judgement of whether the linear model lateralises the
438 reverberant stimulus to the correct direction (negative d' values denote negative ITDs/left of
439 midline; positive d' values denote positive ITDs/right of midline) and whether this lateralisation
440 judgment is considered significant ($d' > 1$ or $d' < -1$ indicated a significant lateralisation in the
441 right and left directions respectively).

442 *ANOVA and T-test for significant differences in lateralisation*

443 Two-way and three-way ANOVAs are implemented to compare the duration of correct
444 lateralisations (time correctly lateralised = bin duration x number of bins where $d' > 1$) by the
445 hemispheric model of SAM tones with non-zero ITDs in either the rising, peak or falling phases
446 as well as the percentage of the phase including a non-zero ITD. A two-tailed T-test is also
447 performed for 200-Hz carrier SAM tones to compare the effect of MSO neuronal type. For the
448 speech stimulus, a paired two-tailed T-test is performed to compare the frequency of incorrect
449 lateralisations (time incorrectly lateralised = bin duration x number of bins where $d' < -1$) in the
450 linear model with either adapting or non-adapting auditory nerve inputs.

451 Results

452 ***A model MSO neuron driven by adapting SBCs reproduces the frequency-*** 453 ***dependent emphasis of ITD information during rising sound-energy***

454 We first explored the extent to which adaptation at model SBCs in the cochlear nuclei can
455 account for the emphasis of ITDs during the rising energy of modulated sounds in a model
456 MSO neuron (Fig. 2B). Acoustic stimuli to the model were amplitude-modulated binaural beats
457 (AMBBs) (Dietz et al., 2013, 2014), in which binaurally presented tones of a slightly different
458 frequency are modulated in amplitude at a rate equal to the difference in frequency across the
459 two ears, and each cycle of rising and falling sound-energy contains a full cycle of interaural
460 phase disparities. AMBBs (Fig. 2A) centred at 600 Hz, with modulation rates 4 to 64 Hz, were
461 presented to a standard model of peripheral auditory processing (Glasberg & Moore, 1990;
462 Zilany et al., 2014), which drove a nonlinear model of brainstem neurons. The model of
463 peripheral auditory processing includes 24 adapting ANFs: twelve each in the left and right
464 ears, with CF 600 Hz. Each of three distinct model ANFs projects an ipsilateral, excitatory
465 synaptic input to one of the eight (four left, and four right) model SBCs. These model synapses
466 uniformly depress ($u = 0.5$) (Rudnicki & Hemmert, 2017) and recover with a 25-ms time-
467 constant (Wang & Manis, 2008). Each model SBC (Rothman & Manis, 2003c) projects a non-
468 depressing, excitatory synaptic input to a multi-compartment model MSO neuron (Brughera et
469 al., 2013) (with minor adjustments described in Methods), for a total of eight excitatory inputs
470 (Couchman et al., 2010). The model SBCs and MSO neuron are Hodgkin-Huxley-type models
471 (Hodgkin & Huxley, 1952) adjusted to temperature 37°C.

472 Beginning without STP, a nonlinear model including SBCs with very strong, non-depressing,
473 supra-threshold synapses, originally developed for high entrainment (Joris et al., 1994) to
474 account for strong ITD sensitivity in the MSO to unmodulated stimuli (Yin & Chan, 1990),
475 produced only slight adaptation in the spike rates of model SBCs (Fig. 3A, top row). In this
476 condition, model SBCs had excitatory synaptic strength, $\Delta g_{E_{SBC}} = 400$ nS; threshold was 34 nS
477 for a single input from rest, using the same model membrane and faster synapses at 38°C
478 (Rothman & Manis, 2003c). With consistently very strong, supra-threshold synapses in SBCs,
479 a model MSO neuron employing relatively weak synapses ($\Delta g_{E_{MSO}} = 18$ nS) responded
480 strongly to zero ITD, (its pre-determined best-ITD) across the AM cycle: most strongly at peak
481 sound-energy, slightly less strongly during rising energy, and less strongly still during falling
482 energy (Fig. 3A, lower three rows; in a 3-way comparison of spike counts for best-ITD during
483 rising vs. peak vs. falling energy, $P < 10^{-9}$ at each modulation frequency). The synchrony
484 index—a measure of temporal alignment of spikes over the AM cycle (see Methods)—ranged
485 from 0.133 at 4 and 64 Hz to 0.161 at 16 Hz for model SBCs, and from 0.595 (64 Hz, best-ITD
486 at peak) to 0.794 (16 Hz, best-ITD during fall) for the model MSO neuron (Rayleigh statistic, P
487 < 0.001 in all cases). (AMBB stimuli had increasing IPD (positive beat direction): “best-ITD
488 during rise” denotes start-IPD = 270°; “best-ITD at peak” denotes start-IPD = 180°; and “best-
489 ITD during fall” denotes start-IPD = 90°.)

490 We next introduced synaptic depression in slightly supra-threshold synapses (maximum
491 $\Delta g_{E_{SBC}} = 83$ nS) at the model SBCs, which then adapted in their spike rates (Fig. 3B, top row).
492 The model MSO neuron maintains a fixed synaptic strength, $\Delta g_{E_{MSO}} = 36$ nS, consistent with
493 excitatory fibre conductances of 37 ± 4 nS measured *in vitro* (Couchman et al., 2010). In model
494 SBCs, adaptation in spike rate followed a similar time-course across AM rates, such that at
495 low-to-moderate AM rates (4 to 16 Hz) most of the adaptation occurred by the peak in the AM
496 cycle, and at moderate-to-high rates (16 to 64 Hz) gradual adaptation was evident across
497 much of the AM cycle. Consistent with physiological and behavioural data at 600 Hz (Dietz et
498 al., 2014; Hu et al., 2017), the model MSO neuron responded to its best ITD strongly during
499 rising amplitude, weakly to moderately (and broadly) at peak energy, and only weakly during
500 falling energy (Fig. 3B, lower three rows; in this 3-way comparison of spike counts, $P \leq 0.003$
501 at each modulation frequency). Adapting similarly in spike rate to the model SBCs, the model
502 MSO neuron had higher spike counts for best-ITD during rising energy vs. peak energy at 4- to
503 16-Hz modulation ($P < 0.02$), and during peak vs. falling energy at 16- to 64-Hz modulation (P
504 < 0.0025). Synchrony-indices to AM for model SBCs ranged from 0.0485 at 4 Hz to 0.174 at 32
505 Hz; and for the model MSO neuron, from 0.450 (64 Hz, best-ITD during fall) to 0.814 (64 Hz,
506 best-ITD during rise) (Rayleigh statistic, $P < 0.01$ for model SBCs at 4-Hz AM, otherwise $P <$
507 0.001).

508 Consistent with behavioural data at the same 600-Hz sound-frequency, a model including
509 synaptic plasticity at SBCs that in turn drive bilateral inputs to an MSO neuron, responds
510 preferentially to ITDs during the rising energy of sounds. Without this adaptation, the
511 preference for spatial cues during rising sound-energy is absent, suggesting a critical role for
512 monaural input pathways to binaural neurons in emphasising spatial information that is likely to
513 be reliable in reverberant listening conditions.

514 Mechanisms for sensitivity to ITDs conveyed in the TFS of sounds are generally thought to be
515 consistent across sound-frequencies up to 1400 Hz (higher in some non-human species),
516 covering the range over which ITDs in the TFS are discriminable. Therefore, given the
517 emphasis to ITDs during the rising energy of modulated sounds at 600 Hz—concordant with
518 perceptual and brain-imaging data obtained at a similar frequency (Dietz et al., 2013)—we
519 expected a similar emphasis at the lower sound-frequency of 200 Hz. Nevertheless, despite
520 our model implementing identical elements, we observed a very different pattern of results at
521 200 Hz compared to 600 Hz. These differences are consistent with behavioural data (Hu et al.,
522 2017): at 600 Hz, human ITD-sensitivity is strongest during rising energy with progressively
523 less ITD sensitivity for peak and falling energy; but at 200 Hz, ITD sensitivity is strong for both
524 peak and rising energy, and again weak for falling energy.

525 With CFs of the model ANFs now equal to 200 Hz, but otherwise employing the same model
526 with monaural adaptive spike-failures in SBCs, identical to that which emphasised ITDs during
527 the rising energy at 600 Hz, we assessed the relative emphasis of ITD cues in the modulation

528 cycle of a 200-Hz AMBB stimulus, for the modulation rates of 8 and 20 Hz employed by Hu et
529 al. (2017). At 200 Hz, the model SBCs showed slight adaptation in spike rate across the AM
530 cycle (Fig. 4A, top row), less adaptation than at 600 Hz. Spike counts in the model MSO
531 neuron (Fig. 4A, lower three rows) matched the patterns of significance in human ITD-
532 detection for AM stimuli at 200 Hz (Hu et al., 2017): spike counts were slightly higher but not
533 significantly for best-ITD during peak vs. rising energy, and spike counts were significantly
534 different (higher) only for best-ITD at peak energy vs. falling energy ($P = 0.0079$ for modulation
535 at 8 Hz; $P = 0.0014$ for modulation at 20 Hz). Synchrony-indices to AM for model SBCs ranged
536 from 0.0762 at 8 Hz to 0.109 at 20 Hz; and for the model MSO neuron, from 0.433 (20 Hz,
537 best-ITD during fall) to 0.807 (8 Hz, best-ITD during rise) (Rayleigh statistic, $P < 0.001$).

538 Our nonlinear brainstem model with adapting SBCs reproduces the emphasis of rising energy
539 in ITD encoding by MSO neurons at 600 Hz, and is consistent with the shift from very strong
540 human ITD-sensitivity during rising energy at 600 Hz, to strong sensitivity during both peak and
541 rising energy at 200 Hz, and with relatively weak sensitivity during falling energy at both
542 frequencies.

543 ***A hemispheric-difference model including adapting SBCs correctly*** 544 ***lateralises amplitude-modulated stimuli with temporally specific ITDs***

545 To test whether monaural adaptation in combination with a heterogeneous population of MSO
546 neurons (Bondy & Golding, 2018; Remme et al., 2014) is also consistent with behavioural
547 observations (Hu et al., 2017), we employed a neural spiking model of both brain hemispheres,
548 incorporating linear, single-compartment model neurons for computational efficiency in
549 representing the bilateral cochlear nuclei and MSOs (Remme et al., 2014), and generating a
550 neuro-metric measure of lateralisation. Following the model concept of Dietz et al. (2009), two
551 hemispheric channels ('left' and 'right') comprised distinct MSO model neuron populations (50
552 neurons each) whose inputs from 'contralateral' cochlear nucleus (CN) were delayed by 0.125
553 cycles of interaural phase difference (IPD, equal to ITD x frequency) (McAlpine et al., 2001)
554 such that they spiked preferentially for sounds arriving from contralateral spatial locations (Fig.
555 5). The difference in spike rate between hemispheres, calculated (in 5-ms epochs) as a signed
556 d' , was then used as a neuro-metric measure of lateralisation (see Methods) (Devore et al.,
557 2009; McAlpine et al., 2001). A uniform synaptic depression ($u = 0.55$) (Rudnicki & Hemmert,
558 2017) was implemented independently at each synapse between an ANF and its target SBC of
559 the VCN. Sinusoidally amplitude-modulated (SAM) tones, with non-zero, positive ITDs
560 positioned within the rising, peak, or falling phases of the AM cycle as per Hu et al. (2017), and
561 see above, were presented to the hemispheric-difference model (Fig. 6). As in the behavioural
562 study, the tone frequency (200 Hz or 600 Hz) and the AM rate (8 Hz or 20 Hz) were varied, as
563 was the proportion (20% or 40%) of the AM cycle containing a non-zero ITD.

564 At 600 Hz, model MSO neurons with fast membranes, i.e. akin to the Hodgkin-Huxley-type
565 model, demonstrated a strong sensitivity to the onset ITD, as indicated by the increased
566 number of instances when the AM stimulus containing a (right-leading) +150 μ s ITD in its

567 rising-energy phase was correctly lateralised [$d' > 1$ in any bin was considered a correct
568 lateralisation of a signal from the 'right' (Fig. 6 *pink vertical bands*)]. This ITD sensitivity
569 decreased across the AM cycle reaching a minimum when non-zero ITDs were restricted to
570 the falling-energy phase (Fig. 6 *bottom row*). The trend for onset dominance at 600 Hz was
571 true for both modulation rates (8 Hz and 20 Hz) and when the proportion of the AM cycle
572 containing non-zero ITDs was either 20% or 40% (Fig. 7 *right column*). Notably, in all three
573 portions of the AM cycle, the number of correct lateralisations decreased as the proportion of
574 an AM cycle containing a non-zero ITD was decreased from 40% to 20% (Fig. 7 *right column*,
575 blue).

576 When an amplitude-modulated 200-Hz tone (with a right-leading, non-zero ITD of +300 μ s)
577 was presented to the fast MSO model, the onset dominance observed at 600 Hz was replaced
578 by an increased weighting of ITD cues towards the peak of the AM cycle (Fig. 6). Indeed, the
579 frequency of correct lateralisations at the peak of AM cycles was either equal to (8-Hz AM
580 stimuli) or higher (20-Hz AM stimuli) than that observed at corresponding onset phases (Fig. 7
581 *middle column*). As at 600 Hz, reducing the proportion of the AM cycle containing a non-zero
582 ITD from 40% to 20% also generated fewer correct lateralisations across all AM phases (Fig. 7
583 *middle column*, blue). Although the fast MSO model could reproduce behavioural trends (Hu et
584 al., 2017) at both carrier frequencies, it generated fewer correct lateralisations overall at 200
585 Hz (Fig. 7 *middle and right columns*). We therefore presented the same 200-Hz carrier
586 stimulus to the linear model MSO neurons with slower membrane properties (Fig. 6). This
587 generated a higher number of correct lateralisations overall, while maintaining, or even
588 augmenting, the maximum weighting of ITD at the peak AM energy in all conditions tested
589 (Fig. 7 *left column*).

590 Our hemispheric-difference model, therefore, suggests that a slower, more integrative MSO
591 neuron may assist lateralisation in lower-frequency channels, in particular by extending the
592 extraction of ITD information towards peak energy in the AM cycle, where human ITD
593 detection is best when comparing at 200 Hz across the AM cycle (Hu et al., 2017).
594 Additionally, our model qualitatively matched the behavioural data by demonstrating a higher
595 propensity to lateralise stimuli of either frequency when 40% vs. 20% of the AM cycle
596 contained a non-zero ITD.

597 ***Adapting SBCs improve the ability of a hemispheric-difference model to*** 598 ***lateralise speech in artificial reverberation***

599 If neural adaptation prior to binaural integration contributes to accurate source localisation, we
600 would expect it to aid lateralisation of speech in a reverberant room, by emphasising ITD cues
601 associated with direct sound over reverberation (Fig. 1 *far left*) (Dietz et al., 2014). To test this,
602 speech signals were presented to the neural model of lateralisation under anechoic (non-
603 reverberant) conditions, and simulated reverberant conditions with direct sound and early
604 reflections off virtual walls (Dietz et al., 2014). We then assessed whether the model correctly

605 lateralised the side to which the source was located in the presence or absence of synaptic
606 depression in SBCs of the cochlear nuclei.

607 In the anechoic condition (Fig. 8A), a word token ('church') was presented to the non-adapting
608 hemispheric-difference model from a virtual location 1 metre from the target and 30 degrees to
609 the right of the midline. The speech waveform—gammatone-filtered at 600 Hz (Fig. 8A *top*
610 *row*)—was more intense at the right ear (red), and led the left-ear signal (blue) by an average
611 ITD of +363 μ s (Fig. 8A *top row*, dark grey). This generated a larger response from model
612 neurons in the 'left' MSO (Fig. 8A *middle row*) and multiple bins throughout the speech token
613 where d' values were > 1 (Fig. 8A *pink vertical bands*), indicating that the talker was correctly
614 lateralised to the right in the non-adapting hemispheric-difference model.

615 In the reverberant condition, the same word token was presented to the non-adapting
616 hemispheric-difference model from the same angle and distance, however it was also followed
617 by two delayed copies generated by early reflections off virtual walls added behind, and to the
618 left of, the listener (Fig. 1B *far left*). This mixture of sound arriving direct from the source and
619 early reflective copies led to a more complex waveform (including a more intense signal at the
620 'left ear' (direct-to-reverberant ratio: -4dB; mean ILD: -3 dB)) whose running ITDs fluctuated
621 between extremely large positive and negative values, culminating in an average IPD of +155°,
622 a value that can easily lead to wrong-side lateralization for sine-tones (Yost, 1981). Although
623 the resulting d' output exceeded 1 in eleven epochs coinciding with waveform onsets (Fig. 8B,
624 *left, pink vertical bands*), it was also briefly lower than -1 in the opposite direction during three
625 intermediate epochs (Fig. 8B, *left, blue vertical bands*), indicating a potentially ambiguous left-
626 right localisation output.

627 We then introduced synaptic depression to the monaurally driven inputs from ANFs to the
628 cochlear nuclei of the hemispheric-difference model, and presented the same reverberant
629 stimulus (Fig. 8B). Despite the potentially confounding ITD (and ILD) cues (Fig. 8B *top row*),
630 adding adaptation in the monaural input pathways enhanced the performance of the binaural
631 model MSO neurons, and generated correct lateralisations of the true source to the right: the d'
632 output exceeding 1 in six time bins without ever crossing below -1 (Fig. 8B *bottom row, right*).
633 When the number of incorrect lateralisations was tallied over a hundred presentations of the
634 reverberant stimulus (Fig. 8C), incorrect lateralisations were observed five times less
635 frequently when synaptically depressing auditory nerve inputs were included in the
636 hemispheric-difference model (mean incorrectly lateralised time for non-depressing synaptic
637 inputs = 6.75 ± 0.50 ms/presentation vs. mean incorrectly lateralised time for depressing
638 synaptic inputs = 1.3 ± 0.24 ms/presentation). This neuro-metric profile agrees with the
639 psychoacoustic percept as has been previously described for similar word tokens (Dietz et al.,
640 2014), suggesting that monaural adaptation increases the weighting of spatial information
641 during rising sound-energy to improve lateralisation of ethological sounds in reverberant
642 environments.

643 Discussion

644 ***The adapting brainstem suppresses responses to late-arriving reverberant*** 645 ***sound while encoding spatial cues***

646 Localising sound-sources in reverberant environments is critical to prey and predator alike, and
647 improves communication in human listeners. Despite reflections from acoustically opaque
648 surfaces degrading spatial cues, localisation must remain accurate. Hypothesising that
649 adaptive brainstem mechanisms suppress responses to late-arriving reverberant sound, thus
650 emphasising early-arriving sound direct from the source for the encoding of spatial cues, we
651 computationally explored the contribution of monaural brainstem adaption to binaural sound-
652 source lateralisation. In our models, accurate lateralisation in reverberation is enhanced by
653 adapting SBCs in the VCN, which project bilaterally to the MSO, a site of primary binaural
654 integration. We show that pre-binaural adaptation can account for the observed ability of MSO
655 neurons to respond preferentially to ITDs conveyed during the early, rising-energy portion of
656 low-frequency sounds near 600 Hz (Dietz et al., 2014). Reflecting perception of normal-hearing
657 listeners at 500 Hz (Dietz et al., 2013), our models successfully glimpse TFS-ITD cues
658 conveyed during the AM cycle's rising portion, suppressing spatial information conveyed in all
659 later portions, including that with highest energy.

660 ***Pre-binaural adaptation with appropriate temporal properties supported the*** 661 ***reproduction of in vivo MSO responses***

662 Our model MSO neurons reproduced *in vivo* responses to AMBBs (Dietz et al., 2014), using
663 pre-binaural adaptation at model ANFs (Zilany et al., 2014, 2009) and SBCs. Adaptive effects
664 of glycinergic inhibition at SBCs *in vivo* (Keine & Rübsamen, 2015; Keine et al., 2016; Kuenzel
665 et al., 2011, 2015) are phenomena-logically modelled using STP as measured *in vitro* at
666 calyceal synapses from ANFs to SBCs (Oleskevich et al., 2000; Wang & Manis, 2008; Yang &
667 Xu-Friedman, 2009, 2015), noting their nearly identical temporal properties: the time-constant
668 of decay in glycinergic inhibition, 23.9 ms (Kuenzel et al., 2015); and the time-constant of
669 recovery in STP, 25 ms (Wang & Manis, 2008). Acknowledging the disputed role of STP, its
670 similar time-course for adaptation compared with glycinergic inhibition supported modelling of
671 *in vivo* MSO responses to AMBB stimuli.

672 Actual STP *in vivo* is reportedly weak due to GABA_B-receptor-mediated limitation of pre-
673 synaptic vesicle release, maintaining initially weaker but more consistent synapses, including
674 slightly supra-threshold calyces (Chanda & Xu-Friedman, 2010; Keine et al., 2016; Kuenzel et
675 al., 2011; Lorteije et al., 2009). Accordingly, STP was not required at model MSO neurons.
676 Significant adaptation on a 25-ms time-scale is not expected to originate at MSO neurons *in*
677 *vivo*: glycinergic inhibition is faster (time-constant, 2 ms) (Magnusson et al., 2005); GABA
678 presumably limits STP, and GABA_B-receptor-mediated synaptic adaptation is slower (time-
679 scale, 500 ms) (Stange et al., 2013).

680 Inhibition at SBCs may not entirely explain pre-binaural adaptation: *in vivo*, some bushy cells
681 (BCs) adapt similarly with and without pharmacological blocking of either glycinergic or GABA_A
682 inhibition (Gai and Carney, 2008). Spike-rate adaptation in ANFs (Zilany and Carney, 2010)
683 can also temporally shape monaural inputs, as suggested by examples of increasing onset-
684 emphasis from adapting model ANFs to globular BCs, for AM rates up to 64Hz (Stecker,
685 2020). Number, synaptic strength, and CF-span of ANF inputs to BCs likely influence how ANF
686 adaptation contributes to pre-binaural adaptation overall (Ashida et al., 2019; Brughera et al.,
687 1996; Carney, 1990, 1992; Rudnicki & Hemmert, 2017).

688 ***Frequency-dependent emphasis of early-arriving sound reflects natural*** 689 ***frequency-profiles in reverberant energy***

690 Natural outdoor acoustics have seemingly influenced brain mechanisms that suppress
691 responses to reverberation. In many outdoor environments, including forests, fields, and
692 streets, reverberation-time ('T60'—the time for reverberant energy to fall by 60 decibels)
693 decreases as sound-frequency decreases below 1500 Hz (Traer & McDermott, 2016).
694 Reflecting this frequency-profile in reverberation-time, our models are consistent with the
695 frequency-dependent behavioural emphasis of ITD during rising and peak sound-energy (Hu et
696 al., 2017), by increasing the weighting of peak energy with decreasing low frequency where
697 reverberation is less energetic. Applying identical parameter values in our Hodgkin-Huxley-
698 type model MSO neuron as sound-frequency decreased from 600 to 200 Hz, model neurons
699 transitioned from responding preferentially to ITDs during rising energy at 600 Hz, to
700 responding equally strongly to ITDs during rising and peak energy at 200 Hz. At both
701 frequencies, model neurons aptly responded only weakly to ITD during falling energy, when
702 direct sound is most likely to be corrupted by reverberation. This is consistent with listening
703 behaviour: at 600 Hz, human listeners are more sensitive to ITDs conveyed during rising-
704 energy than to ITDs at the energy peak; at 200 Hz, listeners are equally sensitive to ITDs
705 conveyed during rising and peak energy; listeners are least sensitive to ITD during falling
706 sound-energy at both sound-frequencies. These data, and our models, suggest that spatial
707 auditory brain mechanisms transmit reliable information, and suppress unreliable information,
708 accounting for natural frequency-profiles in reverberant energy.

709 At very low frequencies, including 200 Hz, where reverberant energy in natural, outdoor
710 scenes is low, suppression of spatial information during peak energy is less important.
711 However, in modern, indoor listening environments, characterised by enclosures with highly
712 reflective walls, reverberation can be high even at very low frequencies. Indoor reverberation,
713 weakly suppressing neurons, and increasing perceptual thresholds for ITD at sound-
714 frequencies below 500 Hz (Brughera et al., 2013), may all contribute to the observed low
715 perceptual weighting of very low frequencies when localising broadband sound (Ihlefeld &
716 Shinn-Cunningham, 2011). This consistent perceptual down-weighting for localisation,
717 presumably by brain centres above the brainstem, occurs even as these very low sound-

718 frequencies contain and apparently convey vital speech information, including the fundamental
719 frequency, and first formant of vowels.

720 Contrasting the weak suppression of late-arriving sound and weak reverberation at 200 Hz,
721 with the strong suppression at 600 Hz and increasing reverberation with higher sound-
722 frequency up to 1500 Hz, suggests the possibility that the human brainstem effectively
723 suppresses responses to reverberation for sound-frequencies from 500 to 1200 Hz, a
724 frequency range that despite being relatively high in reverberation produces the lowest
725 perceptual thresholds for ITD discrimination in human listeners (Brughera et al., 2013; Klumpp
726 & Eady, 1956), and dominates the percept of auditory spatial cues (Ihlefeld & Shinn-
727 Cunningham, 2011; Shinn-Cunningham et al., 1995; Xia et al., 2010).

728 ***Model MSO neurons with a plausible range of membrane speeds are*** 729 ***effective at low sound-frequencies***

730 MSO neurons with slower intrinsic properties than typically recorded in principal MSO neurons
731 (though faster than other types of neurons in the central nervous system) indicate some
732 degree of heterogeneity in the nucleus (Bondy & Golding, 2018; Remme et al., 2014). By not
733 expressing more ion channels than required, the slower MSO neurons encode ITD efficiently,
734 realising a cellular energetic advantage. Introducing moderately slow MSO membranes
735 (labelled “Slow MSO”) boosted the hemispheric-difference model’s ability to lateralise 200-Hz
736 signals, especially at their energetic peak, suggesting a functional benefit of these slower
737 membranes at lower frequencies.

738 ***Adapting SBCs enhance correct lateralisation of reverberant speech***

739 Early reflections—those following the direct signal by 50 ms or less (Bradley et al., 2003)—can
740 disrupt low-frequency sound localisation by conveying spurious TFS-ITD cues (Gourévitch &
741 Brette, 2012). Yet normal-hearing listeners can locate sound-sources, including talkers in
742 reverberant environments (Bregman, 1997). By demonstrating that within a hemispheric 2-
743 channel model, the addition of SBC adaptation emphasises ITD cues in sound onsets, our
744 data suggest one means by which complex sounds, including speech, can be reliably
745 lateralised.

746 Whilst our adapting hemispheric-difference model correctly lateralised reverberant speech, this
747 was based on its d' output surpassing a threshold value in only six of the ninety 5-ms bins with
748 a correct ITD cue available. Although this neuro-metric measure may not appear particularly
749 robust, it should be remembered that only the 600-Hz frequency channel was examined for
750 speech lateralisation. Localisation in reverberant conditions and the precedence effect—the
751 suppression of spatial information for late-arriving sounds—both demonstrate strong weighting
752 of cues from 500 to 750 Hz (Ihlefeld & Shinn-Cunningham, 2011; Shinn-Cunningham et al.,
753 1995; Xia et al., 2010), but they also highlight subjects’ inability to localise pure tones in echoic
754 conditions, suggesting that enhanced speech localisation in reverberant conditions involves
755 localisation cues across the low-frequency spectrum. Adding a midbrain stage, where inferior

756 colliculus (IC) neurons receive inputs from MSO neurons across a wide range of CFs, would
757 further test the extent to which adaptation in the VCN improves speech localisation in
758 reverberant environments.

759 ***Post-binaural adaptation***

760 Onset-cue dominance is demonstrated extensively in the precedence effect (Brown et al.,
761 2015; Wallach et al., 1949), where suppression of neural responses to a brief lagging stimulus
762 occurs over a range of delays between leading and lagging stimuli. Future localisation models
763 might involve monaural parallel inhibition that is feedforward from ANFs to dorsal cochlear
764 nucleus (DCN), with the relatively complex DCN inhibiting the VCN (Keine et al., 2017; Zheng
765 & Voigt, 2006a, 2006b). A broader model with these adaptive brainstem elements, combined
766 with additional inhibitory echo-suppressive mechanisms, such as delayed inhibition to the
767 midbrain (Burger & Pollak, 2001; Kidd & Kelly, 1996; Pecka et al., 2007), might explore
768 whether these mechanisms act cooperatively in robust onset-ITD processing in reverberant
769 conditions. Brainstem and midbrain mechanisms may combine additively or act independently
770 for different stimuli. At least for ongoing, amplitude-modulated sounds, the emphasis of early-
771 arriving sound in ITD-encoding by MSO neurons, combined with the observed lack of
772 increased emphasis at the IC (Dietz et al., 2014), suggests that brainstem nuclei contribute
773 significantly to sound-source localisation in reverberation.

774 ***Early-arriving spatial cues for bilateral cochlear-implant (bCI) listeners***

775 Although listeners with bCIs are most sensitive to ITD during peaks in sound-energy (Hu et al.,
776 2017), acoustically the most accurate ITD-information for source location occurs during rising
777 sound-energy (Dietz et al., 2013). To maximise ITD sensitivity, and provide spatial information
778 that emphasises sound-sources, bCI processors can, during peak energy, provide pulse bursts
779 that overcome adaptation (Srinivasan et al., 2020, 2018) to convey spatial information derived
780 milliseconds earlier during rising energy, from a calculation triggered by the preceding energy-
781 minimum and subsequent energy-increase. Rapidly updating binaural masks (Cantu, 2018)
782 that enhance target sound-sources while preserving spatial cues can also be applied.

783 ***Conclusions***

784 Our models suggest that adaptive brainstem mechanisms contribute to sound-source
785 localisation, emphasising early-arriving sound which is relatively high in direct sound that
786 conveys reliable spatial information during neural encoding, by suppressing responses to late-
787 arriving sound which is relatively high in reverberation. The frequency-dependent emphasis of
788 auditory spatial information conveyed in early-arriving sound is consistent with brain
789 mechanisms that transmit reliable information, and suppress unreliable information. As the
790 auditory brainstem encodes ITDs for determining sound-source locations, its suppression of
791 late-arriving spatial information promotes accuracy and accounts for typical frequency-profiles
792 of reverberant energy in natural outdoor scenes.

793 **References**

- 794 Ashida G, Heineremann HT, & Kretzberg J (2019) Neuronal population model of globular bushy cells
795 covering unit-to-unit variability. *PLoS Comput Biol* 15(12):1–38.
796 <https://doi.org/https://doi.org/10.1371/journal.pcbi.1007563>
- 797 Bondy B, & Golding NL (2018) Variations in intrinsic and synaptic properties in MSO neurons confer a
798 spectrum of ITD sensitivity. ARO Midwinter Meeting, San Diego, CA, USA.
- 799 Bradley JS, Sato H, & Picard M (2003) On the importance of early reflections for speech in rooms. *J*
800 *Acoust Soc Am* 113(6):3233. <https://doi.org/10.1121/1.1570439>
- 801 Bregman AS (1997) *Auditory Scene Analysis - The Perceptual Organization of Sound*. Cambridge,
802 Massachusetts, U.S.A.: M.I.T. Press.
- 803 Brown AD, Jones HG, Kan A, Thakkar T, Stecker GC, Goupell MJ, & Litovsky RY (2015) Evidence for a
804 neural source of the precedence effect in sound localization. *J Neurophysiol* 114(5):2991–3001.
805 <https://doi.org/10.1152/jn.00243.2015>
- 806 Brughera A, Dunai L, & Hartmann WM (2013) Human interaural time difference thresholds for sine
807 tones: The high-frequency limit. *J Acoust Soc Am* 133(5):2839–2855.
808 <https://doi.org/10.1121/1.4795778>
- 809 Brughera AR, Stutman ER, Carney LH, & Colburn HS (1996) A Model with Excitation and Inhibition for
810 Cells in the Medial Superior Olive. *Audit Neurosci* 2:219–233. Retrieved from
811 [https://www.urmc.rochester.edu/MediaLibraries/URMCMedia/labs/carney-lab/codes/Brughera-](https://www.urmc.rochester.edu/MediaLibraries/URMCMedia/labs/carney-lab/codes/Brughera-AuditoryNeuro-1996.pdf)
812 [AuditoryNeuro-1996.pdf](https://www.urmc.rochester.edu/MediaLibraries/URMCMedia/labs/carney-lab/codes/Brughera-AuditoryNeuro-1996.pdf)
- 813 Burger RM, & Pollak GD (2001) Reversible Inactivation of the Dorsal Nucleus of the Lateral Lemniscus
814 Reveals Its Role in the Processing of Multiple Sound Sources in the Inferior Colliculus of Bats. *J*
815 *Neurosci* 21(13):4830–4843. <https://doi.org/10.1523/jneurosci.21-13-04830.2001>
- 816 Cantu M (2018) *Sound source segregation of multiple concurrent talkers via short-time target*
817 *cancellation*. Ph.D. dissertation, Boston University. Retrieved from
818 <https://open.bu.edu/handle/2144/32082>
- 819 Carney LH (1990) Sensitivities of cells in anteroventral cochlear nucleus of cat to spatiotemporal
820 discharge patterns across primary afferents. *J Neurophysiol* 64(2):437–456.
821 <https://doi.org/10.1152/jn.1990.64.2.437>
- 822 Carney LH (1992) Modelling the sensitivity of cells in the anteroventral cochlear nucleus to
823 spatiotemporal discharge patterns. *Philos Trans R Soc Lond B Biol Sci* 336(1278):403–406.
824 <https://doi.org/10.1098/rstb.1992.0075>
- 825 Chanda S, & Xu-Friedman MA (2010) Neuromodulation by GABA Converts a Relay Into a Coincidence
826 Detector. *J Neurophysiol* 104(4):2063–2074. <https://doi.org/10.1152/jn.00474.2010>
- 827 Cherry EC (1953) Some experiments on the recognition of speech, with one and with 2 ears. *JASA*
828 (25):975–979. <https://doi.org/10.1121/1.1907229>
- 829 Couchman K, Grothe B, & Felmy F (2010) Medial Superior Olivary Neurons Receive Surprisingly Few
830 Excitatory and Inhibitory Inputs with Balanced Strength and Short-Term Dynamics. *J Neurosci*
831 30(50):17111–17121. <https://doi.org/10.1523/JNEUROSCI.1760-10.2010>
- 832 Devore S, Ihlefeld A, Hancock K, Shinn-Cunningham B, & Delgutte B (2009) Accurate Sound
833 Localization in Reverberant Environments Is Mediated by Robust Encoding of Spatial Cues in the

- 834 Auditory Midbrain. *Neuron* 62(1):123–134. <https://doi.org/10.1016/j.neuron.2009.02.018>
- 835 Dietz M, Ewert SD, & Hohmann V (2009) Model-based direction estimation of concurrent speakers in
836 the horizontal plane. *J Acoust Soc Am* 125(4):2527.
837 <https://doi.org/https://doi.org/10.1121/1.4783519>
- 838 Dietz M, Marquardt T, Salminen NH, & McAlpine D (2013) Emphasis of spatial cues in the temporal fine
839 structure during the rising segments of amplitude-modulated sounds. *Proc Natl Acad Sci*
840 110(37):15151–15156. <https://doi.org/https://doi.org/10.1073/pnas.1309712110>
- 841 Dietz M, Marquardt T, Stange A, Pecka M, Grothe B, & McAlpine D (2014) Emphasis of spatial cues in
842 the temporal fine structure during the rising segments of amplitude-modulated sounds II: single-
843 neuron recordings. *J Neurophysiol* 111(10):1973–1985. <https://doi.org/10.1152/jn.00681.2013>
- 844 Fischl MJ, Combs TD, Klug A, Grothe B, & Burger RM (2012) Modulation of synaptic input by GABAB
845 receptors improves coincidence detection for computation of sound location. *J Physiol*
846 590(13):3047–3066. <https://doi.org/10.1113/jphysiol.2011.226233>
- 847 Fitzpatrick DC, Kuwada S, Kim DO, Parham K, & Batra R (1999) Responses of neurons to click-pairs
848 as simulated echoes: Auditory nerve to auditory cortex. *J Acoust Soc Am* 106(6):3460–3472.
849 <https://doi.org/10.1121/1.428199>
- 850 Franken TP, Roberts MT, Wei L, Golding NL, & Joris PX (2015) In vivo coincidence detection in
851 mammalian sound localization generates phase delays. *Nat Neurosci* 18(3):444–454.
852 <https://doi.org/10.1038/nn.3948>
- 853 Glasberg BR, & Moore BCJ (1990) Derivation of auditory filter shapes from notched-noise data. *Hear*
854 *Res* 47:103–138. [https://doi.org/https://doi.org/10.1016/0378-5955\(90\)90170-T](https://doi.org/https://doi.org/10.1016/0378-5955(90)90170-T)
- 855 Gourévitch B, & Brette R (2012) The impact of early reflections on binaural cues. *J Acoust Soc Am*
856 132(1):9–27. <https://doi.org/10.1121/1.4726052>
- 857 Haas H (1951) The influence of a single echo on the audibility of speech. *Acoustica* 1(2):49–58.
858 Retrieved from
859 <https://www.ingentaconnect.com/content/dav/aaua/1951/00000001/00000002/art00003>
- 860 Hodgkin AL, & Huxley AF (1952) A quantitative description of ion currents and its applications to
861 conduction and excitation in nerve membranes. *J Physiol* 117:500–544.
862 <https://doi.org/https://doi.org/10.1113/jphysiol.1952.sp004764>
- 863 Hu H, Ewert SD, McAlpine D, & Dietz M (2017) Differences in the temporal course of interaural time
864 difference sensitivity between acoustic and electric hearing in amplitude modulated stimuli. *J*
865 *Acoust Soc Am* 141(3):1862–1873. <https://doi.org/10.1121/1.4977014>
- 866 Hutcheon B, & Yarom Y (2000) Resonance , oscillation and the intrinsic. *Trends Neurosci* 23(5):216–
867 222. [https://doi.org/10.1016/S0166-2236\(00\)01547-2](https://doi.org/10.1016/S0166-2236(00)01547-2)
- 868 Ihlefeld A, & Shinn-Cunningham BG (2011) Effect of source spectrum on sound localization in an
869 everyday reverberant room. *J Acoust Soc Am* 130(1):324–333. <https://doi.org/10.1121/1.3596476>
- 870 Johnson DH (1980) The relationship between spike rate and synchrony in responses of auditory-nerve
871 fibers to single tones. *J Acoust Soc Am* 68:1115–1122. <https://doi.org/10.1121/1.384982>
- 872 Joris PX, Smith PH, Yin TC, & Carney LH (1994) Enhancement of neural synchronization in the
873 anteroventral cochlear nucleus. II. Responses in the tuning curve tail. *J Neurophysiol.*
874 <https://doi.org/10.1152/jn.1994.71.3.1037>

- 875 Joris PX, & Yin TCT (1992) Responses to amplitude-modulated tones in the auditory nerve of the cat. J
876 Acoust Soc Am 91:215–232. <https://doi.org/10.1121/1.402757>
- 877 Keine C, & Rübsamen R (2015) Inhibition shapes acoustic responsiveness in spherical bushy cells. J
878 Neurosci 35(22):8579–8592. <https://doi.org/10.1523/JNEUROSCI.0133-15.2015>
- 879 Keine C, Rübsamen R, & Englitz B (2016) Inhibition in the auditory brainstem enhances signal
880 representation and regulates gain in complex acoustic environments. ELife 5:1–33.
881 <https://doi.org/10.7554/eLife.19295>
- 882 Keine C, Rübsamen R, & Englitz B (2017) Signal integration at spherical bushy cells enhances
883 representation of temporal structure but limits its range. ELife 6:1–16.
884 <https://doi.org/10.7554/eLife.29639>
- 885 Kidd SA, & Kelly JB (1996) Contribution of the Dorsal Nucleus of the Lateral Lemniscus to Binaural
886 Responses in the Inferior Colliculus of the Rat: Interaural Time Delays. J Neurosci 16(22):7390–
887 7397. <https://doi.org/10.1523/jneurosci.16-22-07390.1996>
- 888 Klumpp RG, & Eady HR (1956) Some Measurements of Interaural Time Difference Thresholds. J
889 Acoust Soc Am 28(5):859–860. <https://doi.org/10.1121/1.1908493>
- 890 Kuenzel T, Borst JGG, & van der Heijden M (2011) Factors Controlling the Input-Output Relationship of
891 Spherical Bushy Cells in the Gerbil Cochlear Nucleus. J Neurosci 31(11):4260–4273.
892 <https://doi.org/10.1523/JNEUROSCI.5433-10.2011>
- 893 Kuenzel T, Nerlich J, Wagner H, Rubsamen R, & Milenkovic I (2015) Inhibitory properties underlying
894 non-monotonic input-output relationship in low-frequency spherical bushy neurons of the gerbil.
895 Front Neural Circuits 9(March):1–14. <https://doi.org/10.3389/fncir.2015.00014>
- 896 Lehnert S, Ford MC, Alexandrova O, Hellmundt F, Felmy F, Grothe B, & Leibold C (2014) Action
897 Potential Generation in an Anatomically Constrained Model of Medial Superior Olive Axons. J
898 Neurosci 34(15):5370–5384. <https://doi.org/10.1523/JNEUROSCI.4038-13.2014>
- 899 Liebenthal E, & Pratt H (2002) Human auditory cortex electrophysiological correlates of the precedence
900 effect: Binaural echo lateralization suppression. J Acoust Soc Am 106(1):291–303.
901 <https://doi.org/10.1121/1.427057>
- 902 Litovsky RY, & Yin TC (1998a) Physiological studies of the precedence effect in the inferior colliculus of
903 the cat. I. Correlates of psychophysics. J Neurophysiol 80(3):1285–1301.
904 <https://doi.org/10.1121/1.423072>
- 905 Litovsky RY, & Yin TCT (1998b) Physiological Studies of the Precedence Effect in the Inferior Colliculus
906 of the Cat. II. Neural Mechanisms. J Neurophysiol 80(3):1302–1316.
907 <https://doi.org/10.1152/jn.1998.80.3.1302>
- 908 Lorente De No R (1981) *The Primary Acoustic Nuclei*. New York: Raven.
- 909 Lorteije JAM, Rusu SI, Kushmerick C, & Borst JGG (2009) Reliability and precision of the mouse calyx
910 of Held synapse. J Neurosci 29(44):13770–13784. <https://doi.org/10.1523/JNEUROSCI.3285-09.2009>
- 912 Magnusson AK, Kapfer C, Grothe B, & Koch U (2005) Maturation of glycinergic inhibition in the gerbil
913 medial superior olive after hearing onset. J Physiol 568(2):497–512.
914 <https://doi.org/10.1113/jphysiol.2005.094763>
- 915 Mathews PJ, Jercog PE, Rinzel J, Scott LL, & Golding NL (2010) Control of submillisecond synaptic

- 916 timing in binaural coincidence detectors by K v 1 channels. *Nat Neurosci* 13(5):601–609.
917 <https://doi.org/10.1038/nn.2530>
- 918 McAlpine D, Jiang D, & Palmer AR (2001) A neural code for low-frequency sound localization in
919 mammals. *Nat Neurosci* 4(4):396–401. <https://doi.org/10.1038/86049>
- 920 Moser T, & Beutner D (2000) Kinetics of exocytosis and endocytosis at the cochlear inner hair cell
921 afferent synapse of the mouse. *Proc Natl Acad Sci* 97(1):883–888.
922 <https://doi.org/https://doi.org/10.1073/pnas.97.2.883>
- 923 Nilsson JW, & Riedel SA (2008) *Electric Circuits*. Prentice Hall.
- 924 Oleskevich S, Clements J, & Walmsley B (2000) Release probability modulates short-term plasticity at
925 a rat giant terminal. *J Physiol* 524(2):513–523. <https://doi.org/10.1111/j.1469-7793.2000.00513.x>
- 926 Pecka M, Zahn TP, Saunier-Rebori B, Siveke I, Felmy F, Wiegrebe L, ... Grothe B (2007) Inhibiting the
927 Inhibition: A Neuronal Network for Sound Localization in Reverberant Environments. *J Neurosci*
928 27(7):1782–1790. <https://doi.org/10.1523/JNEUROSCI.5335-06.2007>
- 929 Puil E, Gimbarzevsky B, & Miura RM (1986) Quantification of membrane properties of trigeminal root
930 ganglion neurons in guinea pigs. *J Neurophysiol* 55(5):995–1016.
931 <https://doi.org/10.1152/jn.1986.55.5.995>
- 932 Remme MWH, Donato R, Mikiel-Hunter J, Ballesterro JA, Foster S, Rinzel J, & McAlpine D (2014)
933 Subthreshold resonance properties contribute to the efficient coding of auditory spatial cues. *Proc*
934 *Natl Acad Sci* 111(22):E2339–E2348. <https://doi.org/10.1073/pnas.1316216111>
- 935 Rhode WS (1976) A test for the significance of the mean direction and the concentration parameter of a
936 circular distribution. *Madison Univ Wisconsin Dept Neurophysiol Report*. Retrieved from
937 <http://www.neurophys.wisc.edu/comp/docs/not011/not011.html>
- 938 Rhode WS, & Greenberg S (1994) Encoding of amplitude modulation in the cochlear nucleus of the cat.
939 *J Neurophysiol* 71(5):1797–1825. <https://doi.org/10.1152/jn.1994.71.5.1797>
- 940 Rothman JS, & Manis PB (2003a) Differential Expression of Three Distinct Potassium Currents in the
941 Ventral Cochlear Nucleus. *J Neurophysiol* 89(6):3070–3082. <https://doi.org/10.1152/jn.00125.2002>
- 942 Rothman JS, & Manis PB (2003b) Kinetic Analyses of Three Distinct Potassium Conductances in
943 Ventral Cochlear Nucleus Neurons. *J Neurophysiol* 89(6):3083–3096.
944 <https://doi.org/10.1152/jn.00126.2002>
- 945 Rothman JS, & Manis PB (2003c) The Roles Potassium Currents Play in Regulating the Electrical
946 Activity of Ventral Cochlear Nucleus Neurons. *J Neurophysiol* 89(6):3097–3113.
947 <https://doi.org/10.1152/jn.00127.2002>
- 948 Rudnicki M, & Hemmert W (2017) High Entrainment Constrains Synaptic Depression Levels of an In
949 vivo Globular Bushy Cell Model. *Front Comput Neurosci* 11(March):1–11.
950 <https://doi.org/10.3389/fncom.2017.00016>
- 951 Scott LL, Hage TA, & Golding NL (2007) Weak action potential backpropagation is associated with
952 high-frequency axonal firing capability in principal neurons of the gerbil medial superior olive. *J*
953 *Physiol* 583(2):647–661. <https://doi.org/10.1113/jphysiol.2007.136366>
- 954 Scott LL, Mathews PJ, & Golding NL (2010) Perisomatic Voltage-Gated Sodium Channels Actively
955 Maintain Linear Synaptic Integration in Principal Neurons of the Medial Superior Olive. *J Neurosci*
956 30(6):2039–2050. <https://doi.org/10.1523/JNEUROSCI.2385-09.2010>

- 957 Shinn-Cunningham BG, Zurek PM, Durlach NI, & Clifton RK (1995) Cross-frequency interactions in the
958 precedence effect. *J Acoust Soc Am* 98(1):164–171. <https://doi.org/10.1121/1.413752>
- 959 Smith PH, Joris PX, & Yin TCT (1993) Projections of physiologically characterized spherical bushy cell
960 axons from the cochlear nucleus of the cat: Evidence for delay lines to the medial superior olive. *J*
961 *Comp Neurol* 331(2):245–260. <https://doi.org/10.1002/cne.903310208>
- 962 Srinivasan S, Laback B, Majdak P, & Arnolder C (2020) Improving Interaural Time Difference Sensitivity
963 Using Short Inter-pulse Intervals with Amplitude-Modulated Pulse Trains in Bilateral Cochlear
964 Implants. *JARO - J Assoc Res Otolaryngol*. <https://doi.org/https://doi.org/10.1007/s10162-020-00743-6>
- 966 Srinivasan S, Laback B, Majdak P, & Delgutte B (2018) Introducing Short Interpulse Intervals in High-
967 Rate Pulse Trains Enhances Binaural Timing Sensitivity in Electric Hearing. *JARO - J Assoc Res*
968 *Otolaryngol* 19(3):301–315. <https://doi.org/10.1007/s10162-018-0659-7>
- 969 Stange A, Myoga MH, Lingner A, Ford MC, Alexandrova O, Felmy F, ... Grothe B (2013) Adaptation in
970 sound localization: from GABA B receptor-mediated synaptic modulation to perception. *Nat*
971 *Neurosci* 16(12):1840–1847. <https://doi.org/10.1038/nn.3548>
- 972 Stecker GC (2020) Modeling “Straightness” Versus “Briefness:” Do Adapting Neural Models Account for
973 Temporal Weighting and Bandwidth Effects on Binaural Sensitivity? ARO Midwinter Meeting, San
974 Jose, CA, USA.
- 975 Stimberg M, Brette R, & Goodman DFM (2019) Brian 2, an intuitive and efficient neural simulator. *ELife*
976 8:1–41. <https://doi.org/10.7554/eLife.47314>
- 977 Traer J, & McDermott JH (2016) Statistics of natural reverberation enable perceptual separation of
978 sound and space. *Proc Natl Acad Sci* 113(48):E7856–E7865.
979 <https://doi.org/10.1073/pnas.1612524113>
- 980 Wallach H, Newman EB, & Rosenzweig MR (1949) A precedence effect in sound localization. *Am J*
981 *Psychol* 62(3):315–336. <https://doi.org/https://doi.org/10.1121/1.1917119>
- 982 Wang Y, & Manis PB (2008) Short-Term Synaptic Depression and Recovery at the Mature Mammalian
983 Endbulb of Held Synapse in Mice. *J Neurophysiol* 100(3):1255–1264.
984 <https://doi.org/10.1152/jn.90715.2008>
- 985 Xia J, Brughera A, Colburn HS, & Shinn-Cunningham B (2010) Physiological and psychophysical
986 modeling of the precedence effect. *JARO - J Assoc Res Otolaryngol* 11(3):495–513.
987 <https://doi.org/10.1007/s10162-010-0212-9>
- 988 Yang H, & Xu-Friedman MA (2009) Impact of Synaptic Depression on Spike Timing at the Endbulb of
989 Held. *J Neurophysiol* 102(3):1699–1710. <https://doi.org/10.1152/jn.00072.2009>
- 990 Yang H, & Xu-Friedman MA (2015) Skipped-Stimulus Approach Reveals That Short-Term Plasticity
991 Dominates Synaptic Strength during Ongoing Activity. *J Neurosci* 35(21):8297–8307.
992 <https://doi.org/10.1523/JNEUROSCI.4299-14.2015>
- 993 Yin CT, & Chan JCM (1990) Interaural time sensitivity in medial superior olive of cat. *J Neurophysiol*
994 64(2):465–488. <https://doi.org/10.1152/jn.1990.64.2.465>
- 995 Zheng X, & Voigt HF (2006a) A modeling study of notch noise responses of type III units in the gerbil
996 dorsal cochlear nucleus. *Ann Biomed Eng* 34(4):697–708. <https://doi.org/10.1007/s10439-005-9073-5>
- 997

- 998 Zheng X, & Voigt HF (2006b) Computational model of response maps in the dorsal cochlear nucleus.
999 Biol Cybern 95(3):233–242. <https://doi.org/10.1007/s00422-006-0081-9>
- 1000 Zhou Y, Carney LH, & Colburn HS (2005) A Model for Interaural Time Difference Sensitivity in the
1001 Medial Superior Olive: Interaction of Excitatory and Inhibitory Synaptic Inputs, Channel Dynamics,
1002 and Cellular Morphology. J Neurosci 25(12):3046–3058.
1003 <https://doi.org/10.1016/j.physa.2016.12.040>
- 1004 Zilany MSA, Bruce IC, & Carney LH (2014) Updated parameters and expanded simulation options for a
1005 model of the auditory periphery. J Acoust Soc Am 135(1):283–286.
1006 <https://doi.org/10.1121/1.4837815>
- 1007 Zilany MSA, Bruce IC, Nelson PC, & Carney LH (2009) A phenomenological model of the synapse
1008 between the inner hair cell and auditory nerve: Long-term adaptation with power-law dynamics. J
1009 Acoust Soc Am 126(5):2390–2412. <https://doi.org/10.1121/1.3238250>
- 1010 Zilany MSA, & Carney LH (2010) Power-law dynamics in an auditory-nerve model can account for
1011 neural adaptation to sound-level statistics. J Neurosci 30(31):10380–10390.
1012 <https://doi.org/10.1523/JNEUROSCI.0647-10.2010>
- 1013

Figure Captions

Fig. 1. Reverberant copies of direct speech produce confounding binaural cues. **A** Anechoic speech stimulus ‘church’ (direct sound, without reverberation), spoken at 70 dB SPL by a female talker located +30° to the right and front of a virtual listener. Spectrogram shows speech energy <1 kHz at left ear. Gammatone filters centred at 200 Hz (light grey) and 600 Hz (dark grey) show effects of cochlear filtering on speech waveforms in the left (blue) and right (red) ears. Instantaneous ITDs (light/dark grey) (restricted to $\pm 700\mu\text{s}$, human physiological range) were consistently near +363 μs . **B** Reverberant speech stimulus including direct speech plus two simulated reflections from listener’s left, the first from -65° delayed by 4 ms, and the second from -130° delayed by 8 ms. Reverberant copies increased the energy at the left ear (note the generally brighter spectrogram above 400 Hz). Reverberant energy extends into the quiet pause between the vowel and final consonant (0.45-0.55 ms), generating rapidly varying instantaneous ITDs (also restricted to $\pm 700\mu\text{s}$), along with conflicting ILD cues in the 600-Hz channel

Fig. 2. Amplitude-modulated binaural beats (AMBBs) and the nonlinear brainstem model **A** An AMBB stimulus: the AM rate is set equal to binaural-beat frequency (the difference in frequency between right and left ears). Presented via headphones, interaural phase difference (IPD) cycles through 360° at the same rate as AM. *Start-IPD* (the IPD at zero amplitude) is a free parameter. Shown with right-carrier 616 Hz, left-carrier 584 Hz, AM 32 Hz, and *start-IPD* 270° (right channel trailing by 90°), resulting in zero IPD at the midpoint of rising-amplitude. **B** Nonlinear brainstem model for an MSO neuron and its excitatory inputs, with adaptive spike-failures in SBCs phenomena-logically modelled using synaptic depression. **C** Sub-compartment in the nonlinear brainstem model (see Methods)

Fig. 3. AMBB cycle histograms for nonlinear model brainstem neurons acoustically stimulated by sound-frequencies centred at CF 600 Hz: **A** Without synaptic adaptation, auditory nerve to SBC synapses were strongly supra-threshold. Model SBCs adapted slightly. Model MSO neuron responded to best ITD strongly at peak sound-energy, and slightly but consistently less strongly during rising and falling energy (3-way comparisons, $P < 10^{-9}$). **B** With synaptic adaptation in the cochlear nuclei, the auditory nerve to SBC synapses were supra-threshold at full strength. Model SBCs adapted. Model MSO neuron responded to best ITD strongly during rising energy; weakly to moderately at peak; and weakly during falling, energy (3-way comparisons, $P \leq 0.003$). *Definitions:* Grey silhouettes show the AM envelope. Black lines show static IPD functions. Best-ITD = 0. Best-ITD during rise means *start-IPD* = 270°. Best-ITD at peak means *start-IPD* = 180°. Best-ITD during fall means *start-IPD* = 90°

Fig. 4. AMBB cycle histograms for nonlinear model brainstem neurons stimulated by frequencies centred at CF 200 Hz. Same synaptic adaptation and model SBCs as in Fig. 3B, adapted less at 200 Hz. Same fast model MSO neuron as in Fig. 3B: spike counts were not

1051 significantly different for best-ITD during rising vs. peak energy, and were higher for best-ITD
1052 at peak energy vs. falling energy ($P < 0.01$). *Definitions:* Grey silhouettes show the AM
1053 envelope. Black lines show static IPD functions. Best-ITD = 0. Best-ITD during rise means
1054 *start-IPD* = 270° . Best-ITD at peak means *start-IPD* = 180° . Best-ITD during fall means *start-*
1055 *IPD* = 90°

1056 **Fig. 5.** Overview of the hemispheric-difference model consisting of two MSO populations
1057 (red—left MSO and blue—right MSO), each containing fifty linear, single-compartment model
1058 neurons, with either relatively fast or slow membranes (Remme et al., 2014). Each MSO
1059 neuron model receives four excitatory inputs ‘bilaterally’ from linear, single-compartment model
1060 SBCs of the CN. Three independently-simulated, individually-depressing and medium-
1061 spontaneous-rate model ANFs (Zilany et al., 2014) provide excitatory drive to each SBC model
1062 neuron

1063 **Fig. 6.** Lateralisation by the hemispheric-difference model at 200 Hz and 600 Hz, each with 8-
1064 Hz AM. (A&B) At 200 Hz, both **A** Slow MSO models, and **B** Fast MSO models correctly
1065 lateralised +300 μ s ITDs (top row, black) to the right, based on $d' > 1$ in any 5ms bin (red
1066 vertical bands), most often at peak (middle column) of the AM cycle (grey silhouettes)
1067 compared to rising (left column) and falling (right column) phases (Slow MSO: Rising, 7 bins;
1068 Peak, 12 bins; Falling, 2 bins. Fast MSO: Rising, 3 bins; Peak, 4 bins; Falling, 1 bin); d'
1069 (bottom rows, black) is a difference in mean spike rates between left (top rows, red) and right
1070 (top rows, blue) MSO populations, normalised by variance. The same adapting inputs are used
1071 for both MSO neuronal speeds, therefore more correct lateralisations overall by the Slow MSO
1072 is a result of its slower integration. **C** At 600 Hz, introducing +150 μ s ITD (top row, black)
1073 produced strong onset ITD sensitivity in the Fast MSO during rising phase (left column) that
1074 decreased across the AM cycle (Fast MSO: Rising, 12 bins; Peak, 5 bins; Falling, 1 bin)

1075 **Fig. 7.** Summarising correct lateralisations of SAM stimuli by the hemispheric-difference
1076 model. Mean (\pm SEM) time correctly lateralised per presentation (number of correct
1077 lateralisations * bin duration / 25 presentations) by either Slow MSO neurons at 200 Hz (left
1078 column) or Fast MSO neurons at 200 Hz and 600 Hz (middle and right columns respectively),
1079 for modulation rates of 8 Hz (top row) and 20 Hz (bottom row). ITDs were inserted into either
1080 20% (blue dotted) or 40% (black solid) of the AM cycle during Rising, Peak, or Falling energy.
1081 At 600 Hz, the Fast MSO displays dominant ITD weighting at onset that decreased significantly
1082 across AM cycle (2-way ANOVA, interaction of AM cycle phase x Percentage ITD insertion: 8-
1083 Hz AM, $F(2,48) = 8.310$, $P = 0.001$; 20-Hz AM, $F(2,48) = 50.098$, $P = 0.0001$). At 200 Hz, the
1084 Fast MSO showed equal or better ITD sensitivity at Peak compared to Rising energy (2-way
1085 ANOVA, interaction of AM cycle phase x Percentage ITD insertion: 8-Hz AM, $F(2,48) = 7.83$, P
1086 = 0.001; 20-Hz AM, $F(2,48) = 36.01$, $P = 0.0001$). Slow MSO generated more correct
1087 lateralisations than Fast MSO (2-way ANOVA, interaction of AM cycle phase x Neuron Type:
1088 8-Hz AM, $F(2,48) = 18.82$, $P = 0.0001$; 20-Hz AM, $F(2,48) = 13.12$, $P = 0.0001$) with equal or
1089 augmented ITD sensitivity at Peak for 40% non-zero ITD (Paired two-tailed T-test, Mean Peak

1090 – Rising, $N = 25$: 8-Hz AM, $t(24) = 2.21$, $P = 0.037$; 20-Hz AM, $t(24) = 2.21$, $P = 2.37 \times 10^{-4}$.
1091 Correct lateralisations also increased as the percentage of AM phase containing non-zero ITD
1092 was raised from 20% to 40% (3-way ANOVA, main effect of Percentage ITD insertion: Fast
1093 MSO, $F(1,24) = 418.78$, $P = 0.0001$; Slow MSO, $F(1,24) = 285.622$, $P = 0.0001$)

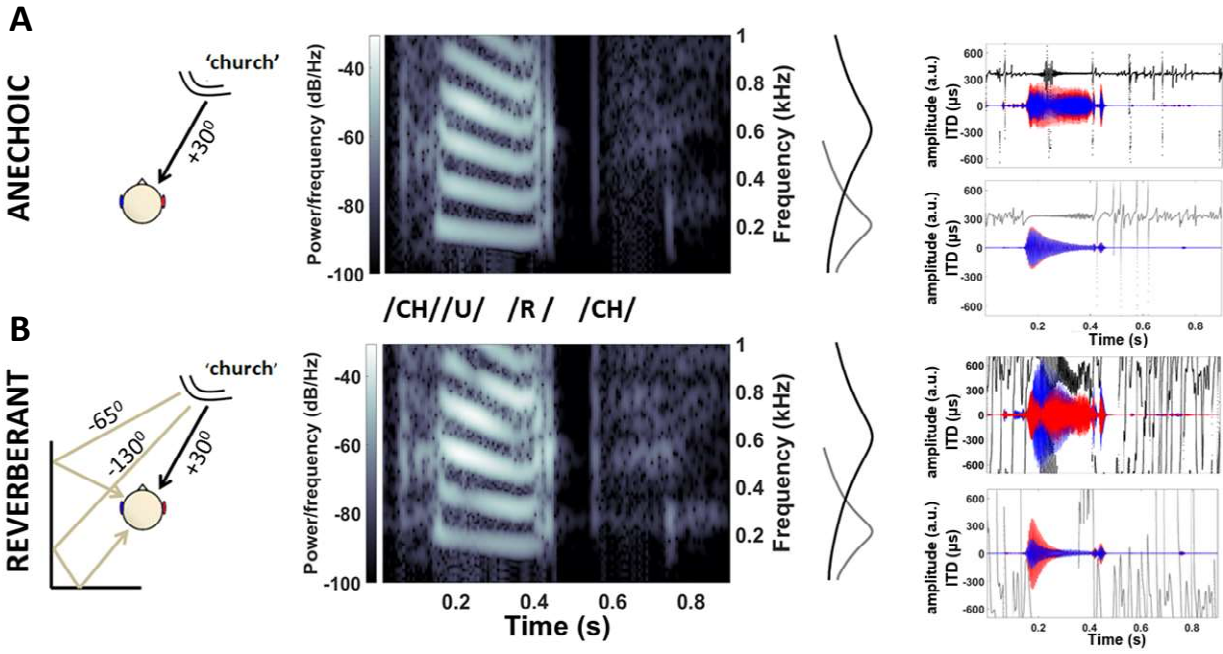
1094 **Fig. 8.** Lateralisation of ‘anechoic’ and ‘reverberant’ speech stimuli by the hemispheric-
1095 difference model (fast MSO, 600-Hz channel) with and without synaptically adapting inputs
1096 from the auditory nerve to the CN: **A** Anechoic stimulus is correctly lateralised to the right (pink
1097 vertical bands) for long periods independently of non-adapting (left column) or adapting (right
1098 column) synaptic inputs. Dry speech stimulus gammatone-filtered at 600 Hz with
1099 instantaneous ITDs (top row), mean firing rates of left (middle row, red) and right (middle row,
1100 blue) MSOs and d' neuro-metric (bottom row) are displayed. **B** Reverberant stimulus requires
1101 adapting synaptic inputs (right column) for correct lateralisations alone (pink vertical bands).
1102 Non-adapting synaptic inputs to the cochlear nuclei produced both correct (left column, pink
1103 vertical bands) and incorrect lateralisations (left column, light blue vertical bands) due to
1104 reverberant stimulus’ highly variable ITDs and confounding ILDs (top row). The inclusion of
1105 synaptic adaptation from the auditory nerve to the cochlear nuclei (using the same auditory
1106 nerve simulations) removes all incorrect lateralisations. Remaining correct lateralisations
1107 correspond with stimulus onsets (right column, pink vertical bands). **C** Quantifying incorrect
1108 lateralisations with non-adapting and adapting synaptic inputs (same auditory nerve
1109 simulations for both) over 100 presentations of the reverberant speech stimulus. Synaptic
1110 adaptation produces a five-fold decrease in incorrect lateralisations ($N = 100$, $t(99) = 9.51$, $P =$
1111 1.31×10^{-15} , two-tailed paired T-test)

1112 **Supplemental Fig. S1.** Somatic membrane impedance magnitude as a function of frequency
1113 in the Hodgkin-Huxley-type model MSO neuron. Injected membrane current is a steady bias
1114 current, plus a frequency sweep in a sine wave with peak amplitude 250 pA. A resonance in
1115 membrane impedance emerges with increases in bias current (I_{BIAS}) and resulting
1116 increases in membrane holding potential (V_{HOLD}): **A** I_{BIAS} 0 pA, V_{HOLD} -60.52 mV, no resonance;
1117 **B** I_{BIAS} 300 pA, V_{HOLD} -59.22 mV, resonance frequency, $f_0 = 408$ Hz; **C** I_{BIAS} 600 pA,
1118 V_{HOLD} -57.88 mV, $f_0 = 513$ Hz; **D** I_{BIAS} 1200 pA, V_{HOLD} -55.24 mV, $f_0 = 692$ Hz. In **B**, slightly
1119 above resting potential, the resonance at 408 Hz indicates a membrane time-constant of $1/(2\pi$
1120 $\times 408$ Hz) = 0.390 ms.

1121

1122

Figures



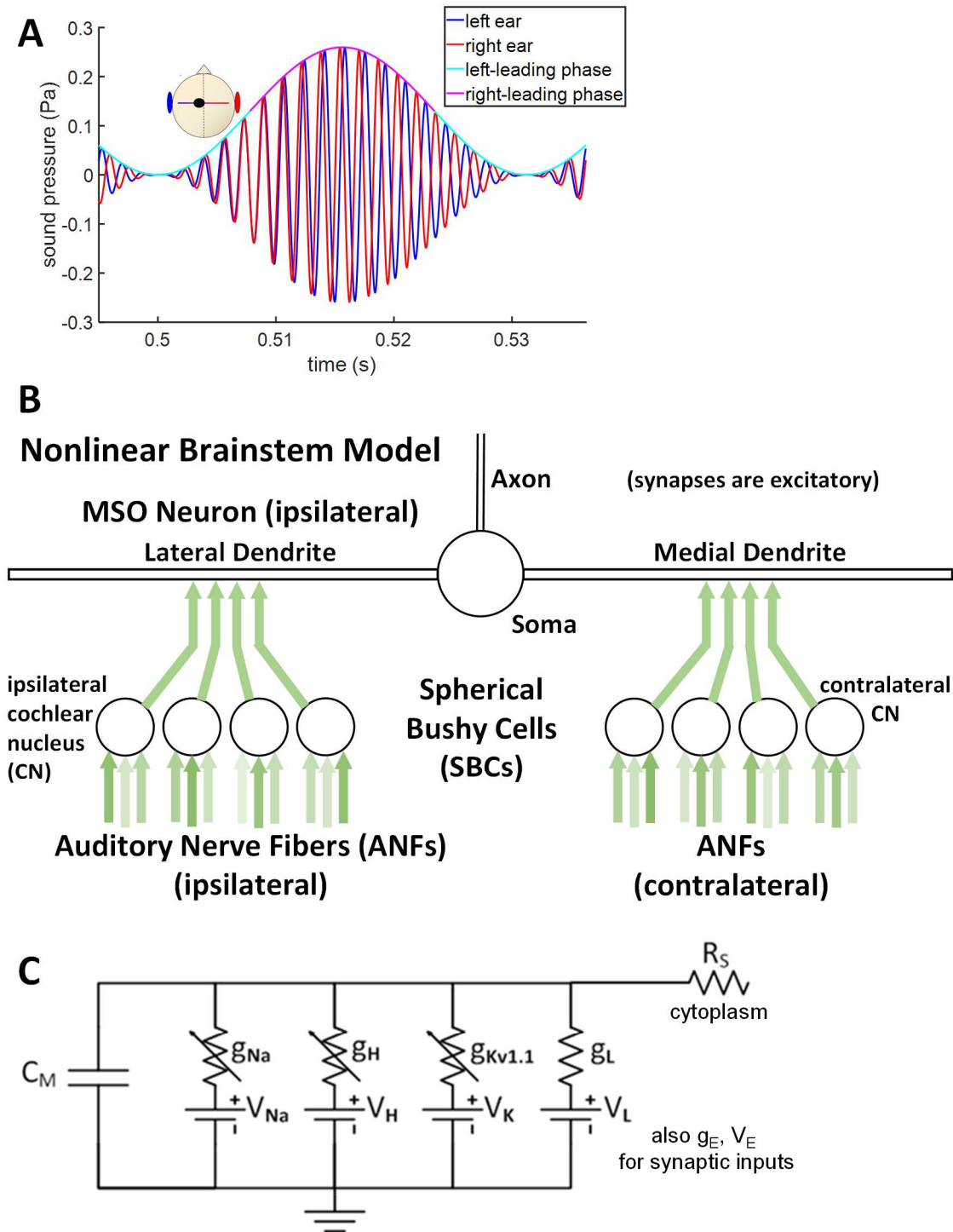
1123

1124

1125

1126 **Figure 1 [in colour, online and in print]**

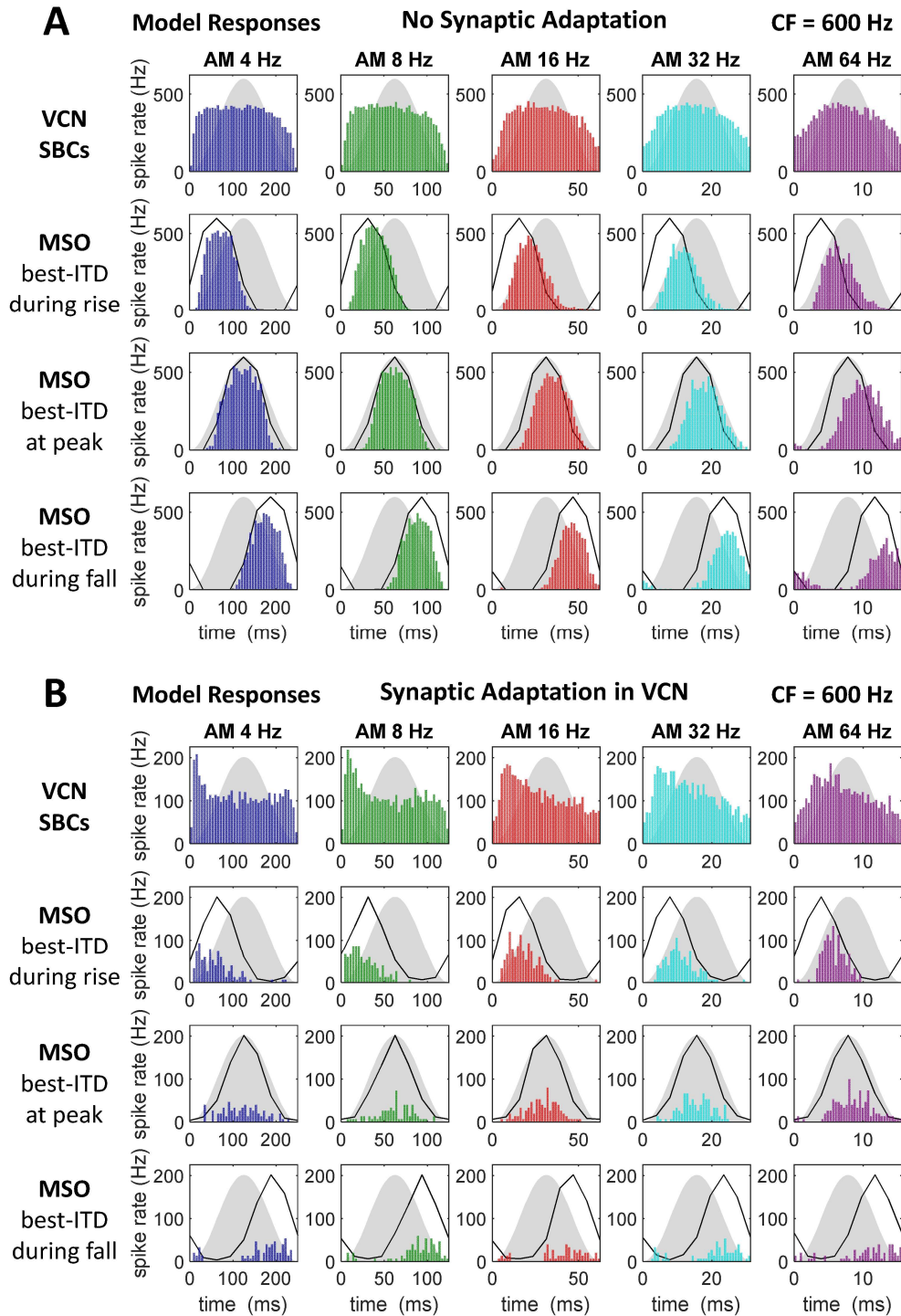
1127



1128

1129 **Figure 2 [in colour, online and in print]**

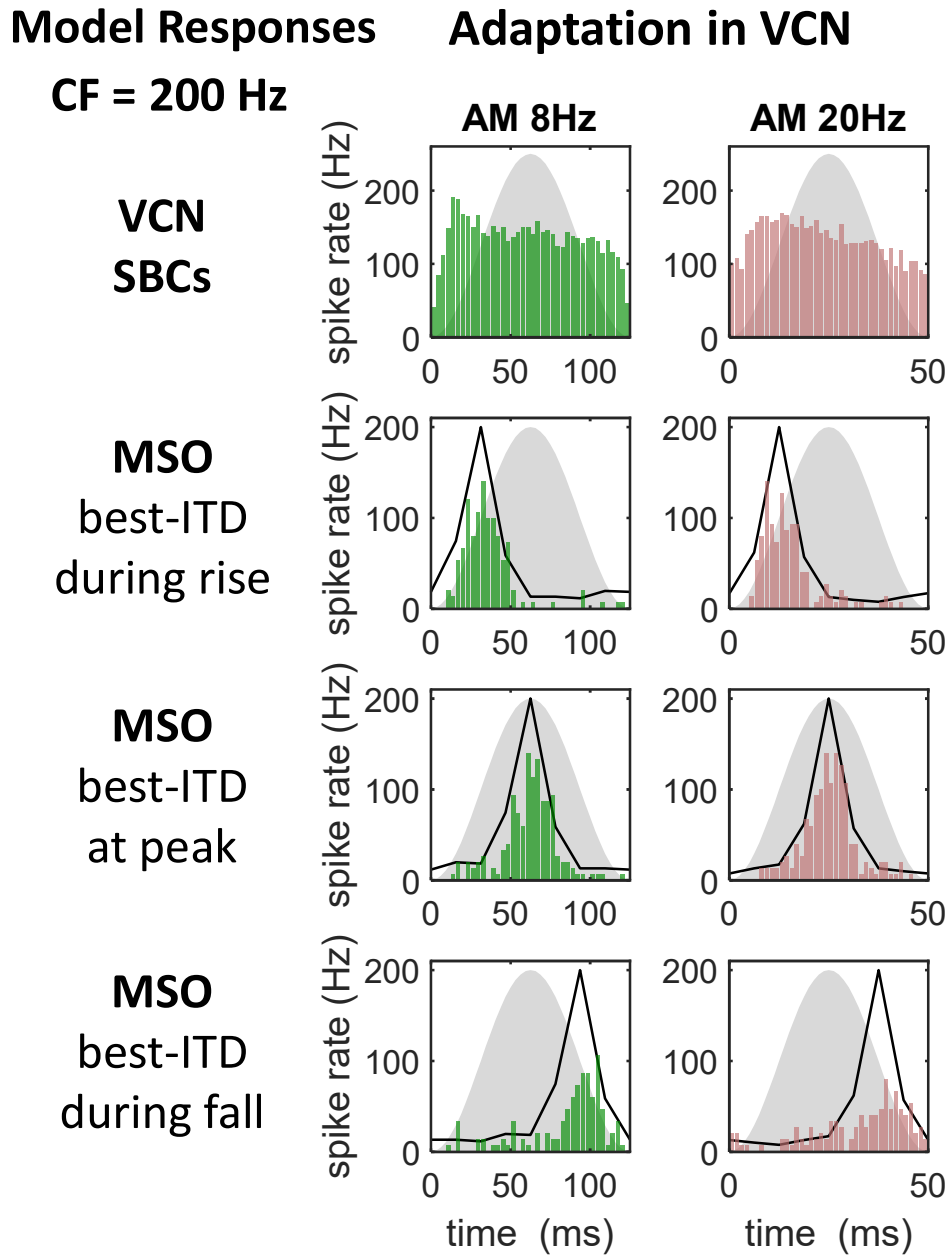
1130



1131

1132 **Figure 3 [in colour, online and in print]**

1133

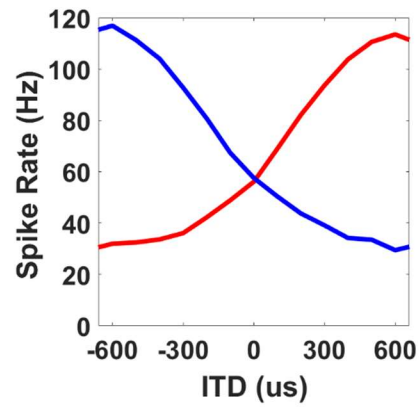


1134

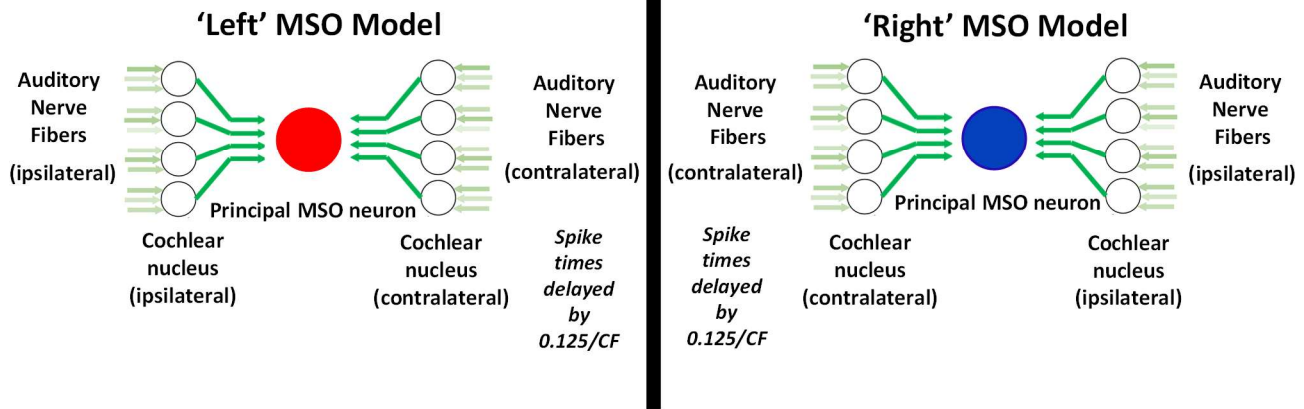
1135

1136 **Figure 4 [in colour, online and in print]**

1137



$$d' = \frac{\mu_{\text{LeftMSO}} - \mu_{\text{RightMSO}}}{\sqrt{\frac{1}{2}(\alpha_{\text{LeftMSO}}^2 + \alpha_{\text{RightMSO}}^2)}}$$

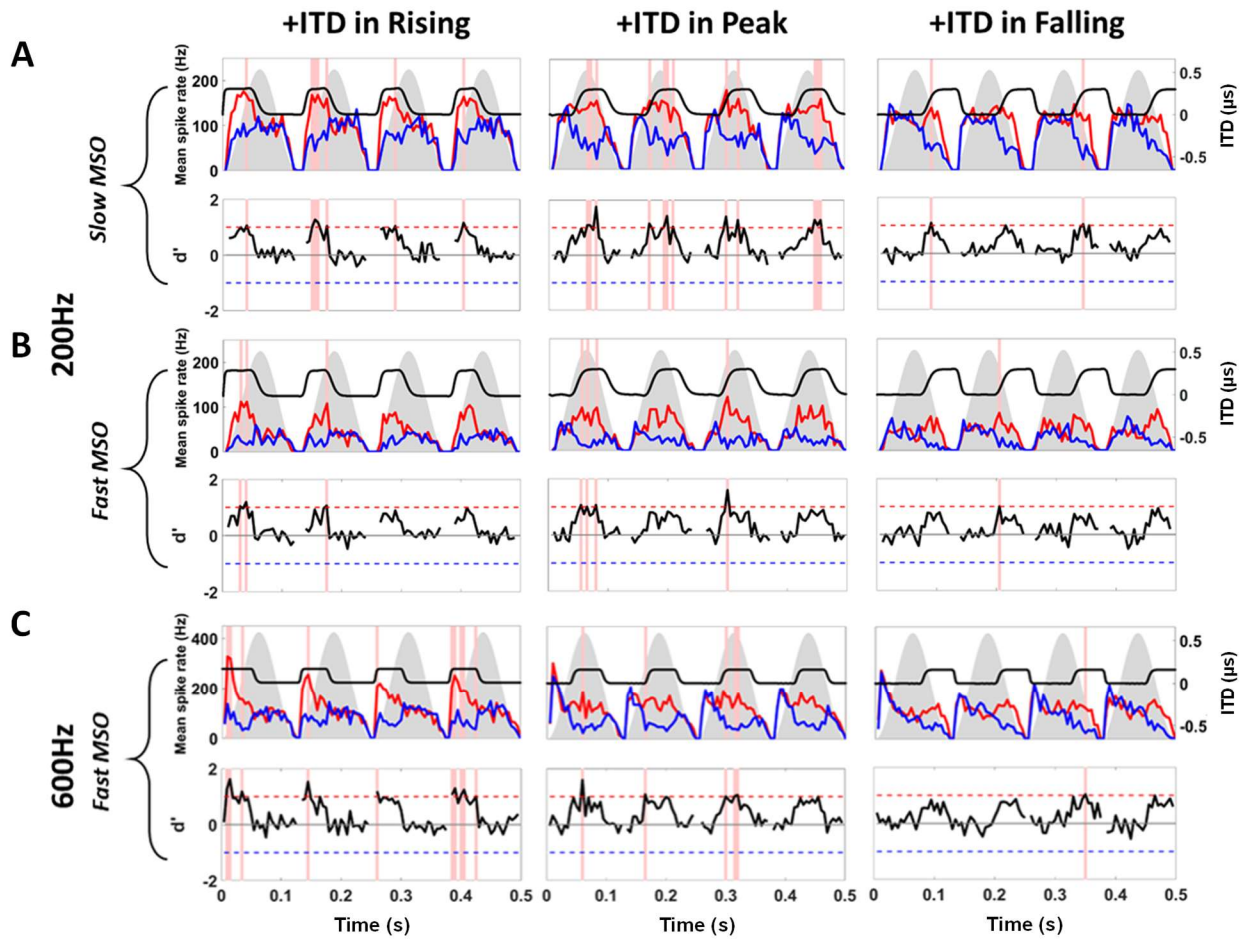


1138

1139

1140 **Figure 5 [in colour, online and in print]**

1141

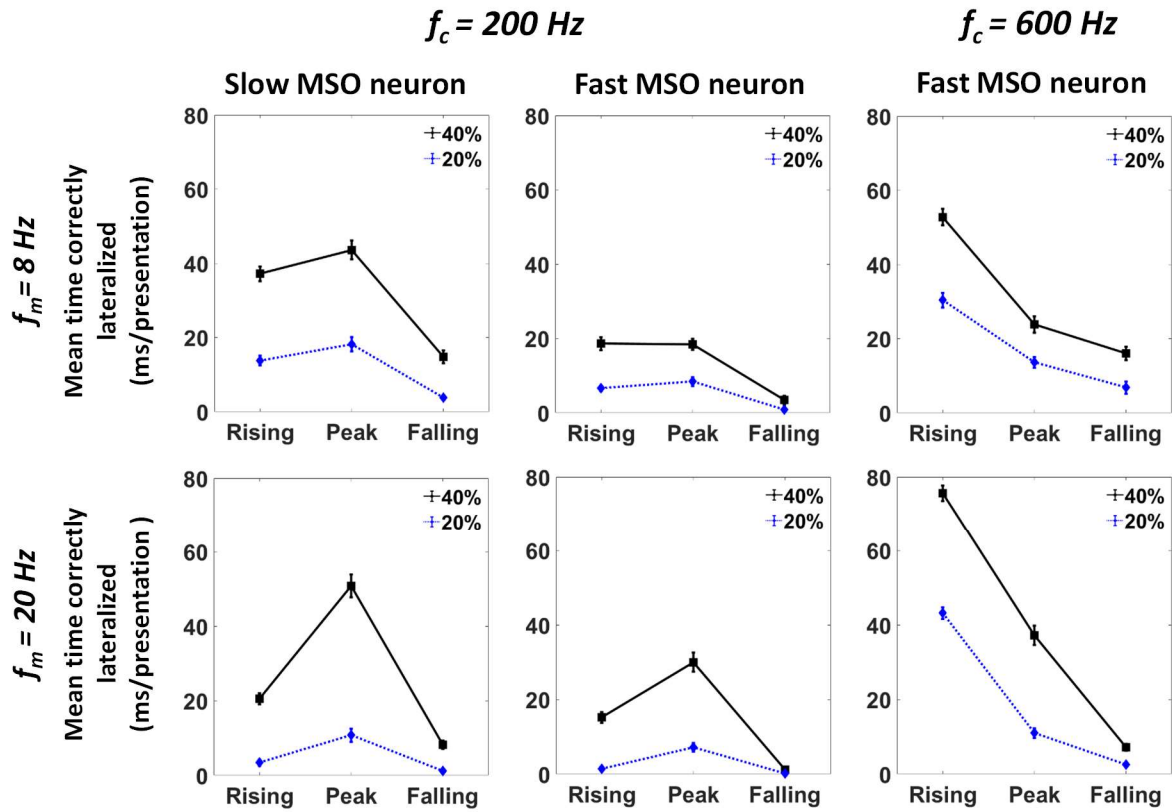


1142

1143

1144 **Figure 6 [in colour, online and in print]**

1145



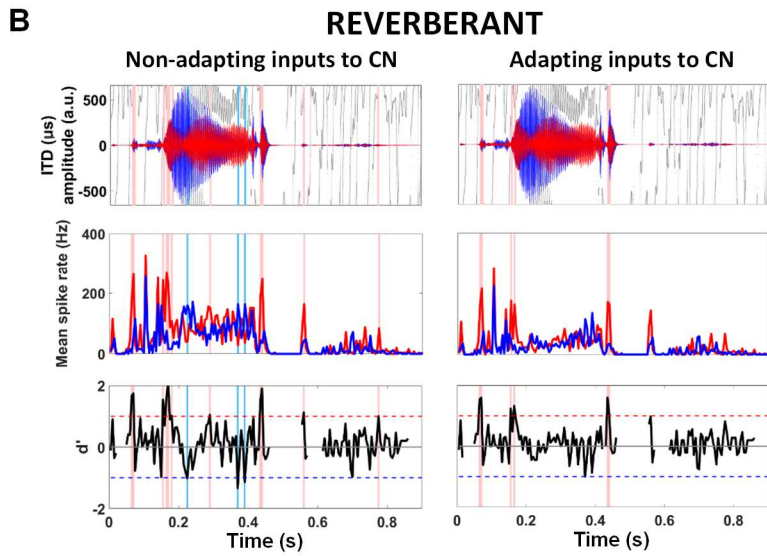
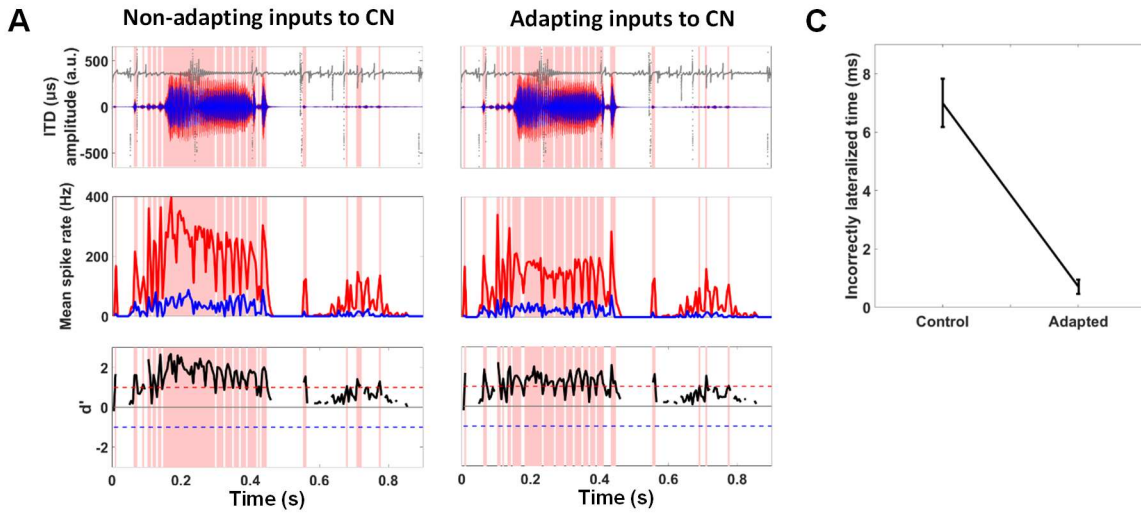
1146

1147

1148 **Figure 7 [in colour, online and in print]**

1149

ANECHOIC

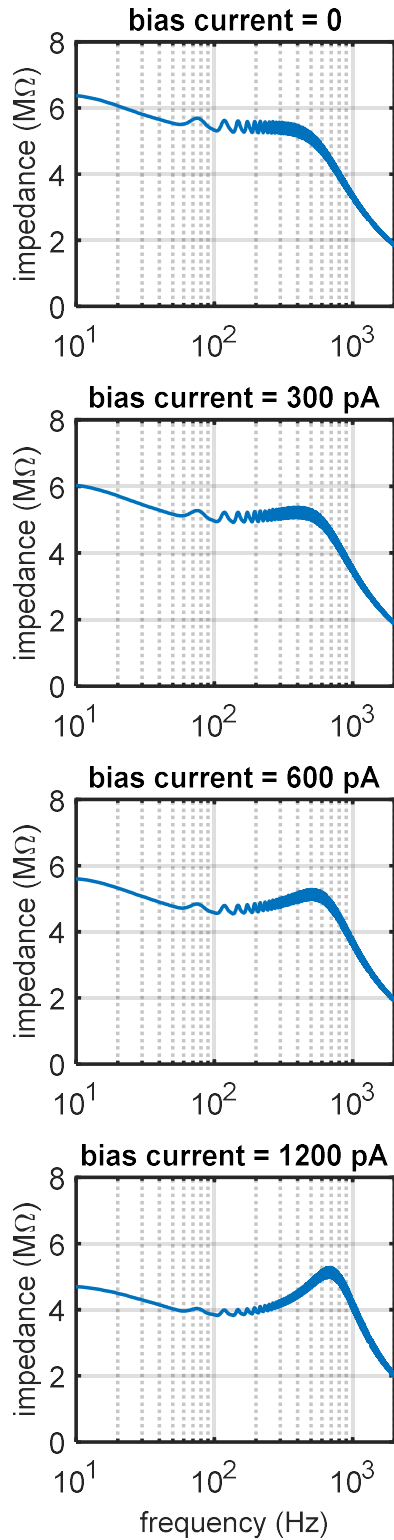


1150

1151

1152 **Figure 8 [in colour, online and in print]**

1153



1154

1155

1156 **Supplemental Figure S1 [in colour]**